Atom probe tomography for isotopic analysis: development of the $^{34}S/^{32}S$ system in sulfides

Phillip Gopon[1,2,3], James O. Douglas[2,4], Frederick Meisenkothen[4], Jaspreet Singh[2], Andrew J. London[2,4], Michael P. Moody[2]

[1]*Dept. of Applied Geosciences and Geophysics, University of Leoben, Leoben, AT, 8700*

[2]*Dept. of Materials, University of Oxford, Oxford, UK, OX1 3PH*

[3]*Dept. of Earth Sciences, University of Oxford, Oxford, UK, OX1 3AN*

[4]*Dept. of Materials, Imperial College London, London, UK, SW7 2AZ*

[4]*Materials Measurement Science Division, National Institute of Standards and Technology, Gaithersburg, MD, USA, 20889*

[5]*UK Atomic Energy Authority, Culham Science Center, Oxfordshire, UK, OX14 3DB*

Abstract

Using a combination of simulated data and pyrite isotopic reference materials, we have refined a methodology to obtain quantitative $\delta^{34}S$ measurements from atom probe tomography (APT) datasets. This study builds on previous attempts to characterize relative $^{34}S/^{32}S$ ratios in gold containing pyrite using APT. We have also improved our understanding of the artefacts inherent in laser pulsed APT of insulators. Specifically, we find the probability of multi-hit detection events increases during the APT experiment, which can have a detrimental effect on the accuracy of the analysis. We demonstrate the use of standardized corrected time-of-flight single-hit data for our isotopic analysis. Additionally, we identify issues with the standard methods of extracting background corrected counts from APT mass spectra. These lead to inaccurate and inconsistent isotopic analyses due to human variability in peak ranging and issues with background correction algorithms. In this study, we use the corrected time-of-flight single-hit data, an adaptive peak fitting algorithm, and an improved deconvolution algorithm to extract $^{34}S/^{32}S$ ratios from the S_2^+ peaks. By analyzing against a standard material, acquired under similar conditions, we have extracted $\delta^{34}S$ values to within ± 5 ‰ (1 ‰ = 1 part per thousand) of the published values of our standards.

1. Introduction

Isotopes are important tracers of geologic processes that allow us to trace a plethora of geochemical pathways, track climate change, and determine the ages of minerals, rocks, and the solar system (Cartwright and Valley, 1991; Spero et al., 1997; Halliday and Lee, 1999). This paper presents a range of instrumental and data processing issues, as well as practical workarounds that allow for the extraction of isotopic data from atom probe data sets of sulfide minerals. Using the analyses of pyrite reference materials as well as simulated datasets as a baseline, we have improved our data acquisition protocols to minimize instrumental artefacts and have refined our data processing algorithms to more accurately and reproducibly extract $^{34}S/^{32}S$ ratios from the S_2^+ family of peaks.

The work was initially developed in order to identify the sources of discreet hydrothermal fluid pulses that are recorded as nanoscale growth zones in gold bearing pyrite (Gopon et al., 2019). As such, the materials we use are related to this application. However, the methodologies developed here are relevant to research investigations far beyond this narrow application, as many of the geochemical processes we aim to track present themselves as similar nanoscale growth zones in minerals (Haase et al., 1980; Schertl et al., 2012; Valley et al., 2015; Boucher, 2018, etc.). Furthermore, the instrumental and data processing artefacts that we have identified will be of interest to anyone who uses atom probe tomography (APT), especially in the measurement of ceramics and other insulating materials (Chen et al., 2009; Thuvander et al., 2011).

The ability to characterize isotopic changes at the nanoscale (and smaller) has the potential to unlock a new level of detail in these geochemical processes. APT is one of the few techniques that can obtain spatially correlated isotopic information at the nanoscale. APT has already

transformed our notions of radiogenic elemental mobility in zircon (Valley et al., 2015; Peterman et al., 2016) and been successfully employed in U/Pb dating (Valley et al., 2014; Fougerouse et al., 2018; Seydoux-Guillaume et al., 2018). Further, isotopic applications in Material Science have been crucial in understanding nuclear fuels (Bachhav et al., 2020; Kautz et al., 2021). However, the application of APT to stable isotopic systems has had limited application (Daly et al.; Gopon et al., 2020; Meisenkothen et al., 2020c). This is primarily due to small isotopic shifts in most of these systems and the relatively large compositional uncertainties often encountered in APT (London, 2019). However, while other mass spectrometry techniques used for geological applications (e.g., Secondary Ion Mass Spectrometry [SIMS]) have low useful ion yields (Hervig et al., 2006), APT has a high combined ionization and detection efficiency of up to 80%. APT, thus, theoretically requires a sampled volume roughly an order of magnitude smaller than that required by other mass spectrometry techniques to achieve a given level of analysis precision (Fougerouse et al., 2020). However, the precision and accuracy of the technique has been hampered by poorly understood instrumental artefacts, complicated mass spectra, isobaric interferences, and operator-induced errors during the data processing (Cairney et al., 2015). If all of these issues can be adequately addressed, then APT genuinely has the potential to unlock new insights into geochemical processes operating at the nanoscale, at precision levels similar to the micrometer-scale techniques currently employed (e.g. SIMS, LA-ICP-MS).

As most geologic materials are insulators, it is usually necessary to use a laser-pulsing mode to induce field evaporation, rather than a voltage pulsing mode (Gault et al., 2012). In this mode, the sample is kept under a localized standing field, and evaporation is instigated through the pulsing of a laser on the sample apex. Experiments are usually operated at a set ion detection rate. To maintain this rate, the standing electric field must be continuously increased to keep a

84 constant evaporation field at the apex of the specimen which gradually blunts over the course of
85 the experiment. The addition of laser-pulsing capability to a commercial local electrode atom
86 probe (LEAP) is a relatively recent feature, and has only been available since 2005 (Bunton et
87 al., 2006). As such, the instrument-associated errors induced are less well understood than with
88 traditional, voltage pulsed, APT. Combine this with the fact that the naturally occurring minerals
89 geologist study are predominantly ionically and/or covalently bonded (with little to no metallic
90 character) (Nesse, 2000), have a tendency to evaporate as complex polyatomic molecules rather
91 than individual ions, and are generally more chemically complex than synthetic materials. All of
92 these factors have made the generation and interpretation of high precision datasets that much
93 more difficult. The main challenges for accurate quantification thus lie in correcting the
94 numerous isobaric interferences inherent in these mass spectra (Figure 1; i.e. S_2^{++} on S^+, Ni on Fe
95 $^{+/++}$, Cu^{++} on S^+, Zn^{++} on S^+, etc.), understanding and correcting for any instrumental biases, and
96 removing errors from the data processing steps.

97 This work is focused on a method to correct the isobaric interferences in the mass spectra of
98 pyrite (FeS_2) to obtain accurate $^{34}S/^{32}S$ ratios, and to shed new light on the instrumental artefacts
99 of laser pulsed APT. We build on the work of Gopon et al. (2019, 2020) and Meisenkothen et al.
100 (Meisenkothen et al., 2020a, 2020c) which provided methods for isotopic analysis using APT.
101 By analyzing a set of well-characterized S isotope standards as well as simulated APT datasets,
102 we have developed a better understanding of the artefacts inherent in laser pulsed APT. Using
103 what we learned to refine our methodology, we are able to not only show relative differences in
104 $^{34}S/^{32}S$ (as in (Gopon et al., 2019)) but can now convert these ratios into quantitative $\delta^{34}S$ ratios
105 by running against known reference materials acquired under similar APT run conditions. This
106 standard-based APT analysis allowed us to accurately determine $\delta^{34}S$ in pyrite to within ~5 ‰

(expressed in parts per thousand difference from a standard; Coplen, 1993). This new capability for APT has wide-ranging applications: including forensics, nuclear fuels, cosmochemistry, ore geology, bio-geochemistry, and igneous and metamorphic petrology.

2. Methods

A set of pyrite isotopic reference materials were provided by Dr. Brian Beard (University of Wisconsin). These reference materials, called Ruttan and Balmat pyrite, were previously characterized by Crowe and Vaughan (1996), and have been routinely used as S isotope reference materials (Hauri et al., 2016; Tanner et al., 2016; Walters et al., 2019). Individual grains of each of the reference materials were mounted in resin in a standard 25 mm round. The grains were then polished in a series of successively finer polishing steps using diamond suspensions, ending with a 1 μm final polish. The samples were then coated with a 20 nm thick carbon coating, to ensure conductivity in the scanning electron microscope (SEM), and transferred into a Zeiss Crossbeam 540 dual beam Focused Ion Beam (FIB)-SEM, located in the David Cockayne Centre for Electron Microscopy at the University of Oxford.

A standard FIB-SEM sample preparation protocol was followed (Thompson et al., 2007), in order to fabricate the highly sharpened needle shaped specimens required for APT. Care was taken to have the final polished needles maintain, as close as possible, a constant initial tip radius and shallow shank angle (<10° shank angle and ~22 nm initial tip radius). Samples were run on the CAMECA LEAP 5000 XR located within the Atom Probe Group of the University of Oxford Department of Materials. APT experimental conditions were based on previous analyses of pyrite (Gopon et al., 2019), but purposefully iterated to observe the influence of different run conditions on the data quality. The instrument was also operated in the “constant charge-state” mode, where instead of increasing the voltage to maintain a constant detection rate, the voltage

and laser energy are adjusted to maintain a constant ratio in the frequency at which charge-states for a specific ion are observed (in our case S^+ at 32 Da and S_2^+ at 64 Da).

For reference we report the Fe^{++}/Fe^+ charge state ratio (CSR) as well as the multi-hit proportion of each of our datasets. Charge state ratios are related to the electric field the sample experiences during field evaporation and can be an important metric used to reproduce experimental conditions between different samples (Prosa et al., 2017). A direct relationship exists between the CSR and electric field strength, and has been computed for Fe^{++}/Fe^+ but not S^{++}/S^+ (Haycock and Kingham, 1980; Gault et al., 2012). The detected multi-hit percentages were calculated using *.ePOS files generated from reconstructions generated in the Integrated Visualization and Analysis Software (IVAS; v3.8.8) and indicate the percentage of recorded detector hits that originate from multiple detection events (i.e., when more than one hit is associated with a given laser pulse event).

3-D volume reconstructions of the specimens were undertaken using the IVAS (v3.8.8) software package, but the majority of compositional and isotopic data analysis was conducted using a set of purpose-built scripts (see sections 2.1, 2.2). These scripts were primarily used to accurately and reproducibly determine the peak counts as well as to back calculate the starting $^{34}S/^{32}S$ ratio from the S_2^+ peak family. The S_2^+ peak family is used rather than S^+ due to the overlap of S_2^{++} on S^+. The accuracy of these scripts, as well as IVAS, was tested against a series of simulated APT datasets, and the most accurate method was then applied to the datasets acquired on the standards. Each of these methods is described in detail below.

2.1 Determination of peak counts

APT software requires the operator to manually select the range of mass-to-charge-state ratio (m/z) values that define the width of each peak in the spectrum (known as 'ranging' the data). The relative shape and width of a given peak might appear to change due to the number of counts at that peak (i.e. the more counts the wider the peak appears), the operating conditions of the machine (i.e. higher laser pulse energy generally results in wider peaks), and the evolution of the voltage curve over the course of an APT experiment. Hence, this manual ranging leads to a source of uncertainty and impacts the reproducibility of the technique (Haley et al., 2015; Blum et al., 2018; Exertier et al., 2018). It should be noted that this uncertainty has a small effect when calculating the major elemental composition of a material. However, since this study is focused on determining S isotopic ratios to a higher level of accuracy than most APT analyses, it is necessary to minimize this user artefact.

To test and to minimize user induced uncertainty in ranging, various protocols (standard ranging, constant ranging, Gaussian fit, and adaptive peak fitting) were developed/adapted to facilitate accurate and repeatable determination of peak counts with minimal user input. Full descriptions of these methods follow.

2.1.1 "Standard" Ranging by eye

The most commonly used method of data reduction is the commercial IVAS software and ranging "by eye" to determine an appropriate region that corresponds to a specific peak. The "decomposition" tool in IVAS can then be used to determine the background corrected counts for the defined range. Alternatively, the MATLAB script package 'AtomProbeLab' (https://sourceforge.net/projects/atomprobelab/) can be used to extract these counts.

To test the precision and reproducibility of this method and the differences between IVAS and AtomProbeLab, we asked three experienced APT users to range and process simulated APT datasets as they saw fit. No guidance beyond this was given other than for the user to apply their "normal" ranging protocol, and the authors were not told how the user "normally" determines ranges. After the data were processed, the test subjects were asked to describe their ranging protocol. User 1 used wide ranges that started just left of the peak and ended where the next peak began. User 2 used narrower but near-constant width ranges and iterated the center of the range after visually inspecting the background determination subjectively for accuracy until the background was deemed acceptable. User 3 used wide ranges that started just before the peak and continued until it intercepted the global background or, if the global background was not reached, until the beginning of the next peak was reached.

These ranges were then processed through the IVAS "decomposition" tool as well as AtomProbeLab to determine the background corrected counts for each peak range. Details of the background correction algorithms built into IVAS and Atom Probe Lab can be found in (Larson et al., 1999) and on the AtomProbeLab website (https://sourceforge.net/projects/atomprobelab/). Full details of the ranges used are reported in Appendix A.

2.1.2 Constant ranging

In AtomProbeLab, range widths are given by a start (pre-peak width) and end (post-peak width) which have units of $\sqrt{\text{Da}}$. If pre- and post-peak widths are the same, say 0.01 $\sqrt{\text{Da}}$, and the peak is at 30 Da, then the m/z range bounds are given by:

$$30 - 0.01 * \sqrt{30} = 29.945 \text{ Da}$$

And

$$30 + 0.01 * \sqrt{30} = 30.055 \text{ Da}$$

This gives a range scaling which is constant in time-of-flight space, since time of flight is directly proportional to the square root of m/z. The peak positions are given by the theoretical isotopic masses from tabulated elemental data.

2.1.3 Gaussian fit

The adaptive peak fitting approach assumes all isotopic variants within a single ion species share the same peak form. The assumption has been supported by empirical observations on several different materials. Once the assumption is made, the important measurement parameter is the peak height, not the integrated peak area, since the area will scale in direct proportion to the peak height. Therefore, alternative peak fitting methods that accurately assesses the relative peak heights of the isotopic variants could yield analysis results with comparable accuracy. For the corrected time-of-flight (TOF) spectra encountered in the present work, the peaks of interest are generally well separated and the upper half of the peaks (Full Width at Half Maximum, FWHM) can be modeled approximately by a Gaussian function, particularly for the single-hit spectra. Generally, the continuum contribution under each peak - the combined background and adjacent overlapping tails - was approximated by a linear model. For the Gaussian peak fitting script, the analyst chooses a range of corrected TOF values that contains the peak of interest. Either one or two additional ranges are chosen adjacent to the specified peak range, as appropriate, for use in the linear regression model and estimation of the continuum contribution that must be subtracted away from under the peak. After the continuum contribution is removed from the peak, the script uses a non-linear least squares algorithm to fit a Gaussian function to the region of the peak spanned at the FWHM. The summit intensity for the peak is then reported as the output and used in the isotopic analysis.

2.1.4 Adaptive peak fitting

Experimental observations have shown the isotopic variants of an ion species - e.g., $^{32,32}S_2^+$, $^{32,33}S_2^+$, $^{32,34}S_2^+$, $^{32,36}S_2^+$, $^{33,33}S_2^+$, $^{33,34}S_2^+$, $^{33,36}S_2^+$, $^{34,34}S_2^+$, $^{34,36}S_2^+$, $^{36,36}S_2^+$ - have nominally the same peak form (Meisenkothen et al., 2020c, 2020a, 2020b). The local spectrum in the region of the family of peaks can thus be approximated as a linear combination of the individual constituent peaks, and an optimization algorithm can be used to determine the "best fit" shape, shared in common by the peaks, and the relative intensities of the peaks. The method has been described as "adaptive peak fitting," because the peak form is not assumed *a priori*. Rather, the algorithm uses an iterative approach to solve for the common peak form, channel by channel, by minimizing the residual sum of squares as a cost function. We are currently using the limited-memory Broyden-Fletcher-Goldfarb-Shanno algorithm with box constraints (L-BFGS-B (Byrd et al., 1995)) to perform the optimization in our analyses. The box constraints are necessary to ensure all solutions are non-negative and to reduce fitting artifacts. A detailed outline of an earlier version of the adaptive peak fitting code is provided in Meisenkothen et al. (2020c). The background spectrum under the family of peaks was assumed to be a constant and was approximated by averaging the ion counts in hundreds of bins immediately to the left of the family of peaks. Adaptive peak fitting has been used successfully to provide repeatable and accurate isotopic analyses with filtered single-hit corrected TOF spectra collected for a variety of materials on a LEAP-4000XSi instrument (Meisenkothen et al., 2020c, 2020a, 2020b). All of our analyses performed with the adaptive peak fitting used corrected TOF spectra exported from the IVAS (v 3.8.8) Cal/Recon Wizard (i.e., timing signal-only-based data, prior to hit finding and ion feedback filtering) with a bin width of 0.01 ns. Prior work has demonstrated the ion data recorded in the IVAS Cal/Recon Wizard corrected TOF spectrum can differ significantly from

that recorded in the *.ePOS file, and the most accurate isotopic analysis results were achieved by employing a consistent analysis methodology on the single-hit corrected TOF data (Meisenkothen et al., 2020c, 2020a, 2020b). Similarly, for silicon specimens of natural isotopic abundance, Prosa and Oltman (2021) have reported their most accurate isotopic analysis results were obtained with non-default RHIT files that had been generated without prompt ion feedback filtering of multi-hit events and by using consistent automated ranging strategies.

The analysis of the S_2^+ peaks is challenging for the current generation adaptive peak fitting algorithm. The proximity of each peak to its neighbors means the algorithm has little information upon which to draw as it tries to "learn" what the underlying spectrum should be beneath each peak. Therefore, box constraints are used to impose upper and lower bounds within which a solution must be found over a specified range of corrected TOF values. Fortunately, the empirical S_2^+ peaks we have encountered thus far are generally well separated, so cascading overlapping peak tails need not be solved by the fitting algorithm and accurate peak forms can be determined.

2.2 $^{34}S/^{32}S$ deconvolution algorithms

Because of the isobaric interference of S_2^{++} on the four stable S^+ isotope peaks (i.e., 32 Da, 33 Da, 34 Da, 36 Da), as well as the interferences of O^+, OH^+, and H_2O^+ on the S^{++} peaks, the only place in the mass spectrum where there is a complete set of sulfur peaks without interference is at the S_2^+ location (64 Da, 65 Da, 66 Da, 67 Da, 68 Da, 69 Da, 70 Da, 72 Da; Figure 1). However, the multiple combinations of sulfur isotopes ($^{32}S+^{32}S\rightarrow$64 Da, $^{32}S+^{33}S\rightarrow$65 Da, $^{33}S+^{33}S\rightarrow$66 Da, $^{32}S+^{34}S\rightarrow$66 Da, $^{33}S+^{34}S\rightarrow$67 Da, $^{32}S+^{36}S\rightarrow$68 Da, $^{34}S+^{34}S\rightarrow$68 Da,

262 $^{33}S+^{36}S \rightarrow 69$ Da, $^{34}S+^{36}S \rightarrow 70$ Da, and $^{36}S+^{36}S \rightarrow 72$ Da) that can comprise the molecules in the
263 S_2^+ family of peaks, makes extracting the $^{34}S/^{32}S$ ratios difficult. To determine the relative
264 amounts of ^{32}S, ^{33}S, ^{34}S, and ^{36}S that contributed to the observed 64 Da, 65 Da, 66 Da, 67 Da, 68
265 Da, 69 Da, 70 Da, and 72 Da peaks, three methods were developed and tested (Monte Carlo,
266 Multinomial, and Linear Least Squares). Due to experimental considerations, only the 64 Da, 65
267 Da, 66 Da, 67 Da, and 68 Da peaks were considered in these calculations.

268 *2.2.1 Estimating isotope abundance: Monte Carlo approach*

269 The Monte Carlo approach, which was previously developed for relative $^{34}S/^{32}S$ comparisons
270 and is described in more detail in Gopon et al. (2019, 2020), was applied here to attempt to
271 simulate the random combinations of sulfur ions during the analysis and make up the peaks in
272 our data. This is achieved by populating two data tables with the same proportion of the numbers
273 32, 33, 34, and 36, with each table representing one of the S atoms in an S_2^+ ion. These values
274 are initially in the proportions of a representative natural isotopic abundance of S (De Laeter et
275 al., 2003); i.e. 94.99 % of the numbers are 32, 0.75 % of the numbers are 33, 4.25 % of the
276 numbers are 34, and 0.01 % of the numbers are 36. A value is randomly pulled from each table,
277 then summed, and input into a third table. This is repeated 10^8 times, and the values in this third
278 table approximate what a mass spectrum using this isotopic abundance would be, assuming that
279 the combination of ions is totally random. We then compare the relative counts for each peak in
280 this table to the values measured from the actual dataset and obtain a mismatch value for the
281 simulated and real data.

282 A grid search of isotopic guesses is then conducted, iteratively changing the abundance of ^{32}S,
283 ^{33}S, ^{34}S, and ^{36}S over the range of naturally occurring isotopic abundances (McKeegan and
284 Leshinv, 2001; Meija et al., 2016), and calculating the corresponding values of 64 Da, 65 Da, 66

Da, 67 Da, 68 Da, 69 Da, 70 Da, and 72 Da for each combination of S isotopes. We define the best-fit combination as the one that minimizes the sum of squared residuals between the observed values and measured values of only the 64 Da, 65 Da, 66 Da, 67 Da, and 68 Da peaks (as the 69 Da, 70 Da, and 72 Da peaks are either indistinguishable from the noise in the mass spectra and/or have an overlap from Fe_2S^{++}). It should be noted that equal weight is given to the mismatch value for each peak no matter its size or relative amounts of ^{34}S and ^{32}S that it might contain– i.e. the model assumes it is equally important to fit the low count peaks and the high count peaks.

The entire process is repeated a total of ten times, increasing the number of guesses over the same search area (decreasing size of each search 'bin'), and averaged to ensure that the global, rather than a local, minimum is output as the best solution. The time required to run the initial iteration is on the order of tens of minutes, with each iteration taking exponentially longer and the final iteration taking a few hours. The full code, average of ten repetitions, takes roughly 8 hours of computing (using personal computer with a 2.8GHz processing speed).

2.2.2 Estimating isotope abundance: multinomial distribution solution

To work around the large amounts of processing time required for the Monte Carlo approach alternative analytical solutions were developed. The following analytical solution is based on a multinomial distribution.

The probability, P, of a certain set of outcomes in a given number of events, using the multinomial distribution, is given by the following equation.

(1) $$P = \frac{n!}{(n_1!)(n_2!)(n_3!)(n_4!)} p_1^{n_1} p_2^{n_2} p_3^{n_3} p_4^{n_4}$$

Here, "n" is the total number of events (in our case, two, because we are drawing pairs of atoms), "n_i" is the number of times outcome "i" occurs; "p_i" is the probability of outcome "i" (in this case, "p" is the relative isotopic abundance), and "i" corresponds to a specific mass number (i.e., 32, 33, 34, 36). For example, for an ion having a (m/z) of 65 Da ($^{32,33}S_2^+$), the expression would simplify to

(2) $$P_{32/33} = \frac{2!}{(1!)(1!)(0!)(0!)} p_1^1 p_2^1 p_3^0 p_4^0 = 2p_1 p_2$$

For the mass peaks composed of several different diatomic sulfur ions, such as the peak at 66 Da ($^{32,34}S_2^+$ and $^{33,33}S_2^+$), equation (1) needs to be evaluated for each constituent type of diatomic sulfur ion and the results summed. We then get a set of five simultaneous equations that can be solved for the four probabilities, p_i, where I_j is the relative empirical intensity observed for each peak in the spectrum (i.e., 64 Da, 65 Da, 66 Da, 67 Da, and 68 Da).

(3) $$p_{32} = \sqrt{I_{64}}$$

(4) $$p_{33} = \frac{I_{65}}{2p_{32}}$$

(5a) $$p_{34} = \frac{I_{66} - p_{33}^2}{2p_{32}}$$

(5b) $$p_{34} = \frac{I_{67}}{2p_{33}}$$

(6) $$p_{36} = \frac{I_{68} - p_{34}^2}{2p_{32}}$$

Two different expressions are produced for p_{34}, the abundance of ^{34}S, and shown as Equations 5a and 5b. Ideally, these two expressions would yield identical results for the ^{34}S abundance. However, since we are empirically estimating p_{34}, the results from these two expressions are

generally not identical – we will thus generate two different values for p_{34}. In our analyses, we have elected to use Equation 5a for estimating p_{34}. Equation 5a is more robust, from a counting statistics standpoint, and exhibits significantly less variability between data sets.

2.2.3 Estimating isotope abundance: non-linear least squares solution

The $^{34}S/^{32}S$ ratio was also calculated using a non-linear least squares solver (MATLAB). The peak intensities of the S_2^+ peaks were calculated using the three most abundant isotopes of S only, with abundances A_1 and A_2 for isotopes ^{32}S and ^{33}S respectively; the ^{34}S isotopic abundance expressed as $1\text{-}A_1\text{-}A_2$. The total counts are expressed as N and this is used to normalize the measured peak counts **r**, which is a vector length 5. The function to optimize is given by the products of the S isotopes contributing to the different S_2 peaks.

$$f(A_1, A_2, N) = \begin{bmatrix} {A_1}^2 \\ 2.A_1A_2 \\ {A_2}^2 + 2.A_1(1 - A_1 - A_2) \\ 2.A_2(1 - A_1 - A_2) \\ (1 - A_1 - A_2)^2 \end{bmatrix} - \frac{r}{N} \quad (7)$$

There are three variables to optimize and ***r*** is a fixed value for any given set of peaks. The optimization goal of the function *f* is to minimize the sum of the squared residuals of each of the items of the resultant vector. Note that MATLAB's 'lsqnonlin' function requires the user-defined function to compute a vector-valued function.

2.3 Tests of peak count determinations and $^{34}S/^{32}S$ deconvolution algorithms

To test the accuracy of the methods used for extracting peak counts (section 2.1) as well as our $^{34}S/^{32}S$ deconvolution algorithms (section 2.2), a series of simulated APT datasets were generated using the MATLAB script of London (London, 2019; https://sourceforge.net/projects/atomprobelab/). In these simulated spectra, we know *a priori* the

345 counts at each of the S_2^+ peaks of interest (hereafter referred to as 'actual' counts), as well as the
346 $^{34}S/^{32}S$ ratio used to create the dataset (hereafter referred to as 'starting' ratio). We, therefore, use
347 the simulated spectra to independently test both the methods for extracting counts and the
348 methods for back calculating the $^{34}S/^{32}S$ ratio. The starting sulfur isotopic abundance used was
349 kept constant (0.0447084; $^{34}S/^{32}S$) for these simulations with only the algorithm used to simulate
350 the peaks being iterated (i.e., with increasing level of complexity). However, it should be noted
351 that uncertainty from counting statistics for our simulated datasets (containing 10 million ions
352 each), means that the 'real' $^{34}S/^{32}S$ ratio might fluctuate by $7x10^{-6}$ (based on a 95% CI).

353 A series of simulations incorporating an increasing level of complexity was implemented such
354 that: Simulation 1 - Delta peak shape with no background; Simulation 2 - Delta peak shape with
355 background (signal to noise = 10); Simulation 3 - Gaussian peak shape with no background
356 (Gauss sigma = 0.072 Da); Simulation 4 - Gaussian with background (signal to noise = 10,
357 Gauss sigma = 0.072 Da); Simulation 5 - Gaussian with background (signal to noise = 10, Gauss
358 sigma = 0.3 Da); Simulation 6 – 'Real' peak shape with no background; Simulation 7 - 'Real'
359 peak shape with background (signal to noise = 10, standard deviation = 0.14 Da); Simulation 8 -
360 'Real' peak shape with background (signal to noise = 10, standard deviation = 0.3 Da). 'Real'
361 peak shape denotes a peak form designed to mimic an empirical peak that may be encountered in
362 an APT spectrum. Spectra of these simulations are shown in Appendix B.

363 *2.4 Delta Notation*

364 In general, isotopic data in the geosciences are reported not as absolute isotopic ratios, due to
365 instrumental issues, but as relative ratios compared to a measured standard. This ratio is referred
366 to as delta notation and in our case is calculated as:

367 (8) $$\delta^{34}\mathrm{S} = 1000\ ‰ \text{ x } \left(\frac{\left({}^{34}S/{}_{32}S\right)_{sample}}{\left({}^{34}S/{}_{32}S\right)_{reference}} - 1 \right)$$

368 The notional zero point for sulfur isotopes is Canyon Diablo troilite (CDT), as it is thought to
369 represent the most primitive ratio in our solar system (0.0450045; Jensen and Nakai, 1962), and
370 analyses are reported compared to that standard. In practice, however, this standard is rarely used
371 and instead a secondary standard which was previously measured against CDT is used as a
372 standard and the data is corrected to the CDT scale by the following formula:

373

374 (9) $$\delta^{34}\mathrm{S\ CDT} = 1000\ ‰ \text{ x } \left(\frac{\left({}^{34}S/{}_{32}S\right)_{sample}}{\left({}^{34}S/{}_{32}S\right)_{reference}} - 1 \right) + \delta^{34}\mathrm{S}_{reference}$$

375 We follow the normal convention with the caveat that we report all simulated data against
376 the notional CDT value (0.045005) using Equation 8 and report the real APT data both against
377 the notional CDT value and by running the two standards against each other using Equation 9.
378 Similar δ^{x}S expressions can be used to quantify the ratio variations in $^{33}S/^{32}S$ and $^{36}S/^{32}S$.
379 However, our focus is on the $^{34}S/^{32}S$ ratio, since this has significance for fluid source
380 fingerprinting in geological applications.

381 ## 3. Results

382 Part of this study was to observe instrumental artefacts inherent in the technique, as well as
383 user induced artefacts that come about during data processing. Table 1 shows the results for four
384 of the simulated data sets and compares the various methods used to measure relative peak
385 intensities. Figure 2 shows the percent difference between the ‘actual’ and the measured relative
386 peak intensities for the same four simulated data sets. Figure 3 provides the corresponding

387 $^{34}S/^{32}S$ ratios for these simulated datasets. As mentioned earlier (section 2.1, 2.2, 2.3), the four
388 simulated datasets represent examples of the easiest (Simulation 1), medium difficulty
389 (Simulation 5), and most challenging analysis situations (Simulation 7 and Simulation 8)
390 provided by the set of eight simulations. The percent difference in Figure 2 is calculated as:

391 (10) $$Absolute\,Value\left(\frac{[actual\ counts]-[measured\ counts]}{[actual\ counts]}\right)*100$$

392 The full results of the various data processing methods applied to all eight of the simulations can
393 be found in Appendix C.

394 Figure 2 shows the large scatter inherent in the different ways of determining peak counts. As
395 Simulation 1 was a delta function with no noise, all methods were able to accurately reproduce
396 the 'actual' counts (zero line). Once more complexity is incorporated into the simulations the
397 methods deviated significantly, especially in their ability to accurately reproduce the 'actual'
398 counts for both the large (ex. 64 Da) and small (ex. 67 Da) peaks. While most of the methods
399 reproduce the large (64 Da) peak reasonably well, the percent difference of the actual versus
400 measured for the smallest peak (67 Da) shows deviations greater than 200 % from the actual
401 (Table 1). The normal ranging 'by eye' approach performed poorly for the Gaussian (Simulation
402 5) compared to the 'real' peaks (signal to noise = 10, st.dev. = 0.14 Da) and is off the scale for
403 Figure 2. However, the worst performance of the 'by eye' approach was on the most realistic
404 simulation (Simulation 8; signal to noise = 10, st.dev. = 0.3 Da). Strangely, the constant range as
405 well as the Gaussian fit reproduced the small peak intensities (67 Da and 68 Da) for the 'real'
406 peak shapes represented by Simulation 7 and Simulation 8 better than the Gaussian distribution
407 represented by Simulation 5 (~350 % deviation for Gaussian fit of the 67 Da peak). The
408 Gaussian fit and adaptive peak fitting produced similar levels of accuracy for the 'real' peak

409 shapes (Simulation 7 and Simulation 8), but the most overall consistent method is the adaptive
410 peak fitting approach.

411 Figure 3 shows the three different approaches for the back calculation of the original $^{34}S/^{32}S$
412 ratio. The Monte Carlo approach was able to get within ~8 ‰ of the correct answer for
413 Simulation 1 but failed to get within 20 ‰ of the correct answer for all other simulations (except
414 when the 'actual' counts were used; Figure 3/Table 1). The multinomial and the linear least
415 squares approaches produced the same results for all methods of peak count determination to
416 within 0.1 ‰ (Table 1) but did deviate from the 'starting' ratio possibly due to the counting
417 statistics inherent in the simulations.

418 Table 2 shows the calculated $^{34}S/^{32}S$ ratios of our empirical datasets from the two pyrite
419 reference materials (Ruttan and Balmat). All $^{34}S/^{32}S$ ratios are calculated using adaptive peak
420 fitting (section 2.1.4) to obtain the relative peak intensities and the multinomial approach to
421 back-calculate the $^{34}S/^{32}S$ ratios (section 2.2.2). Appendix D additionally shows the same data
422 processed by Gaussian fitting and fitting from IVAS. We also report the corresponding $\delta^{34}S$
423 values, which are calculated against the opposite standard acquired under the same APT run
424 conditions (see discussion), i.e. [$^{34}S/^{32}S$.Balmat@40pJ] / [$^{34}S/^{32}S$.Ruttan@40pJ]. Where two of
425 the same standards were acquired under the same run conditions, the standard with the closest
426 dataset number is used (as it is closest in time). Data for the pyrite reference materials were
427 analyzed over a range of laser energies to ascertain the influence on $^{34}S/^{32}S$. The standard data of
428 the two largest datasets (R5083_0893 and R5083_0892) are further subdivided over specific
429 ranges of standing voltage (i.e., time intervals of the analysis) to attempt to isolate the influence
430 that changes during the progression of the run have on the resultant mass spectra and multi-hit
431 fraction. Figure 4 shows the results of the progression of the APT experiment (for dataset

R5083_0893) on the multi-hit fraction. This increase in the multi-hit fraction correlates with a decrease in the Fe^{++}/Fe^{+} (Figure 5) and was noted to influence the resultant $^{34}S/^{32}S$ ratios (Table 2; Figure 6). The influence of the changing standing field (i.e., progression of the run) is most pronounced on the $\delta^{34}S$ calculated against the nominal Canyon Diablo Troilite $^{34}S/^{32}S$ ratio (Equation 8; Figure 6). When the data is compared to a standard acquired using the same analysis conditions (Equation 9) and over the same voltage range the issue becomes less pronounced (Figure 6). When the single hit data over the entire voltage range is used, the best results are obtained and the $\delta^{34}S$ was reproduced to within ~5 ‰ $\delta^{34}S$ of the published values (Crowe and Vaughan, 1996). However, the small number of datasets might mean that this deviation could be larger (for the single-hit or multi-hit data). Note that the 'entire' voltage range is never used, but rather we mean during stable data acquisition (i.e., after the initial calibration and before tip failure).

4. Discussion

The careful analysis of reference materials in this study has given us insight into the challenges of laser pulsed APT, as well as highlighting potential solutions to produce quality data. As shown in Figure 6, when the necessary steps are taken to correct analytical issues, our technique reproduced the published $\delta^{34}S$ values to within ~5 ‰ $\delta^{34}S$.

Rigorous testing of the various methods to determine relative peak intensities and analytical solutions for the back-calculation of $^{34}S/^{32}S$ ratios (Figure 2 and Figure 3) shows that error can be introduced depending on the method of measuring peak intensities. The 'standard' ranging approach is the most inconsistent and inaccurate. This is in part due to the inability of the human observer to be able to visualize parts of the peak that are close to the noise threshold. This was most evident with the approach of User 3, who attempted to use ranges that ended when the peak

reached the global background (unless another peak was reached first). This led to widely different range widths that by eye still looked appropriate. However, it must be noted that the simulations modeled the same peak width regardless of relative peak height (of which the analysts were unaware), so the most appropriate ranging should in fact be one that is at least consistent in its width. Users 1 and 2 did use relatively constant range widths, however the very wide ranges of User 1 meant that more emphasis was placed on the background correction. Table 1 shows that this over-reliance on the accuracy of the background correction schemes for the wide ranges used by User 1 and 3, produces data that can be hugely inaccurate (including zero and negative peak counts; Table 1). Part of the study was to compare different methods of background correction (i.e., those built into IVAS and AP Lab; Larson et al., 1999; London, 2019) and we note large discrepancies between the methods, even when exactly the same ranges are used.

The lower level of accuracy observed in the peak intensity determination by 'standard' ranging has a significant impact on the calculated $^{34}S/^{32}S$, as evidenced by Table 1. Deviations of > 40 ‰ $\delta^{34}S$ were noted in the analytical solutions (multinomial and linear least squares; sections 2.2.2/2.2.3) for the simulated data. It must be noted that the Monte Carlo (section 2.2.1) approach showed large discrepancies in the $\delta^{34}S$ values, when compared to the analytical solutions. This is most likely due to the inability of our Monte Carlo approach to place relative importance on the individual peaks, as the approach comes up with a best fit for all of the peaks, regardless of the magnitude of the contribution an individual peak makes to the $^{34}S/^{32}S$ ratio (i.e., it places equal emphasis on the misfit parameter even if the peak contains no ^{34}S or ^{32}S). The consequence of this is that when the method used to measure relative peak intensities is inaccurate, it has a significant detrimental effect on the Monte Carlo solution. This is most pronounced for the 67 Da

peak which all of the methods had the most issue correctly determining the associated peak counts (Figure 2). The absence of the 67 Da peak from the analytical solution for the ^{34}S abundance found by the multinomial approach and the weighted importance of the larger peaks for the linear least squares approach, means these two methods do not suffer from the same issue. Furthermore, the multinomial and linear least squares approaches, relative to the Monte Carlo method, are less sensitive to any issues related to the determination of relative peak intensities within the S_2^+ family of peaks. The linear least squares and multinomial solutions produce roughly the same results (to within 0.1 ‰ $\delta^{34}S$), and the preference to use the multinomial approach for the remaining data processing is simply because the workflow from the adaptive peak fitting to multinomial is simpler (i.e., the output from one is directly readable by the other).

The influence of instrumental artefacts has been investigated with the detrimental influence of the signal loss to multi-hits being the primary hindrance to obtaining accurate and precise isotopic data. Figure 4 shows that there is an increase in the relative number of multi-hits as the experiment progresses (i.e., as the voltage increases). The progression of the APT experiment has the first order effect of blunting the apex of the sample through field evaporation. This blunting means the laser is exciting a larger surface area, increasing the probability of an ion evaporation event. So, while the standing voltage must be increased to compensate for this blunting effect, the local electric field required for field ionization is actually decreasing (Table 2). This decrease in local electric field as the APT experiment progresses changes the preferential charge state for the evaporating ionic species and has the effect of increasing the multi-hit percentage (Figure 5).

Based solely on counting statistics, it would seem the more counts present in the molecular S_2^+ peaks we are using to determine the $^{34}S/^{32}S$ ratio, the greater the precision, and possibly the

accuracy, should be. However, the opposite trend is apparent in our data (Table 2); though, our assessment may be hampered by the limited number of data sets in our analysis. One possible explanation for this observed trend is the increased number of multi-hit detection events. Multi-hit detection events can suffer from ion signal loss, as a result of detector dead time effects, which tends to produce significant isotopic and chemical measurement bias (Saxey, 2011; Thuvander et al., 2011, 2019; Meisenkothen et al., 2015). If dead-time is a significant factor in introducing bias into our sulfur isotopic measurements, then we would expect the "All Hit" data reported in Table 2 to reflect an undercounting of the major isotope (^{32}S), and thus a relative over counting of the minor isotope (^{34}S). Therefore, $^{34}S/^{32}S$ is expected to be higher for data sets with more multi-hit detection events. In fact, this is roughly what we observe in Table 2. The 3500 V to 4500 V range for dataset 8493 has more multi-hits than the 2500 V to 3500 V range, and it has a higher $^{34}S/^{32}S$. Likewise, the 8462 and 8460 data sets have a higher multi-hit fraction and a higher $^{34}S/^{32}S$, on average, than the 8493 and 11434 data sets. So, while not definitive, these results are consistent with multi-hit data having an impact on our analysis results. Also, the average number of multi-hit detection events in data set 9023 ($^{34}S/^{32}S = 0.0458$) is similar to that for data sets 8462 and 8460 (average $^{34}S/^{32}S = 0.0457$), so we would expect the $^{34}S/^{32}S$ to be comparable for these three data sets, which it is. However, in calculating the $\delta^{34}S$ value, we take a ratio of opposite standards $^{34}S/^{32}S$. Since the opposite standards were collected under similar acquisition conditions, the multi-hit bias is expected to partially cancel out, since the numerator and denominator would be similarly affected by the deadtime effects.

A potential alternative solution to avoid changes in preferential charge state ratio evaporation was considered by using our atom probe in the "constant charge state" mode. The hope was that by maintaining a constant charge state ratio the multi-hit fraction could at least be kept constant

524 during the run and could then be more easily corrected for. However, this data acquisition mode
525 produced some of the largest deviations from the nominal $\delta^{34}S$, possibly because changes in laser
526 energy have a more significant effect on data quality than the voltage evolution.

527 As discussed in section 2.4, isotopic data in the geosciences are often reported relative to a
528 measured standard. However, this comparison of ratios between standards and unknown is
529 difficult in APT, as the primary focusing optic in APT is the sample itself. The diameter of the
530 hemispherical cap and the shank angle of the needle shaped specimen are primarily responsible
531 for the applied electric field (and thus standing voltage) required to field evaporate ions from the
532 sample, and the trajectories that the ions take to the detector. For these reasons, standards based
533 APT has generally been thought of as being impractical, as the artefacts induced by different tip
534 geometries and shapes were thought to be larger than the instrumental artefacts.

535 However, our work shows the opposite is true, i.e., that the instrumental induced artefacts are
536 relatively consistent and considerably larger than those seemingly induced by tip geometries, at
537 least in our sample set where care was taken to produce roughly the same tip geometries (Figure
538 6/Table 2). Samples must therefore be analyzed against a standard, measured under similar APT
539 experimental conditions, and ideally sharpened to a similar tip radius and shank angle as the
540 unknown sample. Confirmation of the lesser influence of the tip geometries is evidenced by the
541 repeat analysis of the same standards from different APT needles (Table 2), which show between
542 tip deviations that are smaller than the absolute deviation from the notional isotopic value for our
543 standards (Figure 6).

544 The increasing standing field has a large effect on the accuracy of our data (Table 2), in a
545 large part, due to the increased likelihood of multi-hits at higher voltages (Figure 4). The analyst
546 must be careful to use data from a standard that is comparable in voltage range and/or data

quality regarding multi-hits. Work is ongoing to better understand and to correct this influence. Several strategies are under consideration, including the use of new detector technology (Kelly, 2020), new laser technology (Chiaramonti et al., 2019), and artificially reducing the detection efficiency to reduce the number of multi-hits (Thuvander et al., 2019). However, the solution presented herein is to only use filtered single-hit data which is processed using adaptive peak fitting from Meisenkothen et al., (2020c). Combining this methodology with a reference material standard acquired under similar conditions (e.g., 80 pJ), produced quantitative results on our reference materials within ± 5 ‰ $\delta^{34}S$ of their published reference values (Crowe and Vaughan, 1996). Considering the difficulty in mathematically assessing the compound influence of counting statistics, instrumental artefacts, and error in our deconvolution solver; we take the measured deviation from the nominal standard ratio (5 ‰ $\delta^{34}S$) using our recommended methodology (standards based APT at 80 pJ of a sample with <10° shank angle and ~25nm tip radius, single-hit corrected TOF spectrum processed with adaptive peak fitting, and multinomial 34/32 calculation) as a preliminary estimate of the total error of our technique.

We should point out that our technique has currently only been tested in relatively pure pyrite (i.e., little or no trace elements) and we caution the application to other sulfide minerals before more thorough testing can be done. The purer the sample is, the less potential for unforeseen isobaric interferences on the peaks used in our technique. A separate protocol was developed to correct for small isobaric interferences of Cu on this family of peaks (Gopon et al., 2019) and would likely need to be expanded upon for more complex sulfides.

5. Conclusion

This study rigorously analyzed simulated and empirical APT data from pyrite reference materials in order to develop a method for determining quantitative S isotopic ratios from APT datasets. We have also obtained a more in-depth understanding of some of the instrumental artifacts (e.g., signal loss due to multi-hits) and data reduction artefacts (produced by inaccurate and inconsistent ranging and background corrections) inherent in laser pulsed APT and have identified issues with the 'standard' methods of APT data reduction built into IVAS and Atom Probe Lab. Using the adaptive peak fitting algorithm from Meisenkothen et al. (2020c), we can accurately and reproducibly extract relative peak intensities which can be converted into $\delta^{34}S$ values using the analytical solutions described in section 2.2. We believe this paper shows some of the major problems and barriers to stable isotopic analysis with APT and how to overcome many of them. We presented a method whereby we have obtained quantitative $\delta^{34}S$ values from APT data of pyrite to 5 ‰ accuracy.

In summary:

- In order to obtain more precise APT data we need to remove human error in ranging. We have used an adaptive peak fitting algorithm (Meisenkothen et al., 2020c) to reproducibly and accurately obtain the counts at each peak without the need to determine a peak range.
- A large issue in obtaining accurate $^{34}S/^{32}S$ data from the APT appears to be due to changes in analysis conditions during an analysis. The increase in voltage appears to cause more multi-hits, which preferentially removes counts of the highest intensity peaks and contributes bias to our APT data.

- Accurate determinations of $\delta^{34}S$ values in pyrite appear to only be possible using known reference materials run as standards under similar acquisition conditions as that used for the unknown.
- Using the approach of standards-based atom probe tomography, run under the same conditions (80 pJ), on samples prepared to similar geometries, and processed in the same way (adaptive peak fitting of the corrected TOF spectra and multi-nominal $^{34}S/^{32}S$ calculation) we were able to obtain the published values of the Ruttan and Balmat pyrite sulfur isotopic standards to within ± 5 ‰ $\delta^{34}S$.

Acknowledgements

The authors would like to acknowledge funding from the following sources. We acknowledge use of characterization facilities within the David Cockayne Centre for Electron Microscopy, Department of Materials, University of Oxford, alongside financial support provided by the Henry Royce Institute [EP/R010145/1]. The Zeiss Crossbeam FIB/SEM used in this work was supported by EPSRC through the Strategic Equipment Fund Grant: EP/N010868/1. AJL was supported by the EPSRC Grant [EP/T012250/1]. The LEAP 5000XR used in this study was funded by an EPSRC Grant [EP/M022803/1].

[†]*Disclaimer*

Certain commercial equipment, instruments, or materials are identified in this paper in order to specify the experimental procedure adequately. Such identification is not intended to imply recommendation or endorsement by the University of Leoben, University of Oxford, National Institute of Standards and Technology, or UK Atomic Energy Authority, nor is it intended to imply that the materials or equipment identified are necessarily the best available for the purpose.

References:

Bachhav, M., Gan, J., Keiser, D., Giglio, J., Jädernäs, D., Leenaers, A., and Van den Berghe, S., 2020, A novel approach to determine the local burnup in irradiated fuels using Atom Probe Tomography (APT): Journal of Nuclear Materials, v. 528, doi:10.1016/j.jnucmat.2019.151853.

Blum, T.B., Reinhard, D.A., Chen, Y., Prosa, T.J., Larson, D.J., and Valley, J.W., 2018, Uncertainty and Sensitivity Analysis for Spatial and Spectral Processing of Pb Isotopes in Zircon by Atom Probe Tomography, *in* Microstructural Geochronology: Planetary Records Down to Atom Scale, p. 327–350.

Boucher, F.R.G.F.G.B., 2018, Population - wide garnet growth zoning revealed by LA - ICP - MS mapping : implications for trace element equilibration and syn - kinematic deformation during crystallisation: Contributions to Mineralogy and Petrology, v. 173, p. 1–22, doi:10.1007/s00410-018-1503-0.

Bunton, J., Lenz, D., Olson, J., Thompson, K., Ulfig, R., Larson, D., and Kelly, T., 2006, Instrumentation Developments in Atom Probe Tomography: Applications in Semiconductor Research: Microscopy and Microanalysis, v. 12, p. 1730–1731.

Byrd, R.H., Lu, P., Nocedal, J., and Zhu, C., 1995, A limited memory algorithm for bound constrained optimization: SIAM Journal on Scientific Computing, v. 16, p. 1190–1208.

Cairney, J.M., Rajan, K., Haley, D., Gault, B., Bagot, P.A.J., Choi, P.P., Felfer, P.J., Ringer, S.P., Marceau, R.K.W., and Moody, M.P., 2015, Mining information from atom probe data: Ultramicroscopy, v. 159, p. 324–337, doi:10.1016/j.ultramic.2015.05.006.

635 Cartwright, I., and Valley, J.W., 1991, Low-18O Scourie dike magmas from the Lewisian
636 complex, northwestern Scotland: Geology, v. 19, p. 578–581, doi:10.1130/0091-
637 7613(1991)019<0578:LOSDMF>2.3.CO;2.

638 Chen, Y.M., Ohkubo, T., Kodzuka, M., Morita, K., and Hono, K., 2009, Laser-assisted atom
639 probe analysis of zirconia/spinel nanocomposite ceramics: Scripta Materialia, v. 61, p. 693–
640 696, doi:10.1016/j.scriptamat.2009.05.043.

641 Chiaramonti, A.N., Miaja-Avila, L., Blanchard, P.T., Diercks, D.R., Gorman, B.P., and Sanford,
642 N.A., 2019, A Three-Dimensional Atom Probe Microscope Incorporating a Wavelength-
643 Tuneable Femtosecond-Pulsed Coherent Extreme Ultraviolet Light Source: MRS Advances,
644 v. 4, p. 2367–2375, doi:10.1557/adv.2019.296.

645 Coplen, T.B., 1993, Reporting of stable carbon, hydrogen, and oxygen isotopic abundances, *in*
646 Proceedings of the fifth IAEA Meeting on Stable Isotope Standards and Intercomparison
647 Materials, p. 31–34.

648 Crowe, D.E., and Vaughan, R.G., 1996, Characterization and use of isotopically homogeneous
649 standards for in situ laser microprobe analysis of 34 S/ 32 S ratios: American Mineralogist,
650 v. 81, p. 187–193, doi:10.2138/am-1996-1-223.

651 Daly, L. et al. Defining the Potential of Nanoscale Re-Os Isotope Systematics Using Atom Probe
652 Microscopy: , p. 0–2, doi:10.1111/ggr.12216.

653 Exertier, F. et al., 2018, Atom probe tomography analysis of the reference zircon gj-1: An
654 interlaboratory study: Chemical Geology, p. #pagerange#,
655 doi:10.1016/j.chemgeo.2018.07.031.

Fougerouse, D., Kirkland, C., Saxey, D., Seydoux-, A.-M., Guillaume, Rowles, M.R., Rickard, W.D.A., and Reddy, S.M., 2020, Nanoscale isotopic dating of monazite: Geostandards and Geoanalytical Research, v. 44, p. 637–652, doi:10.1111/ggr.12340.

Fougerouse, D., Reddy, S.M., Kirkland, C.L., Saxey, D.W., Rickard, W.D., and Hough, R.M., 2018, Time-resolved , defect-hosted , trace element mobility in deformed Witwatersrand pyrite Geoscience Frontiers Time-resolved , defect-hosted , trace element mobility in deformed Witwatersrand pyrite: Geoscience Frontiers, v. 10, p. 55–63, doi:10.1016/j.gsf.2018.03.010.

Gault, B., Moody, M.P., Cairney, J.M., and Ringer, S.P., 2012, Atom Probe Microscopy (Z. M. Hull, R., Jagadish, C., Osgood, R.M. Jr., Parisi, J., Wang, Ed.): New York, v. 1, 411 p., doi:10.1017/CBO9781107415324.004.

Gopon, P., Douglas, J.O., Auger, M.A., Hansen, L., Wade, J., Cline, J.S., Robb, L.J., and Moody, M.P., 2019, A Nanoscale Investigation of Carlin-Type Gold Deposits: An Atom-Scale Elemental and Isotopic Perspective: Economic Geology, v. 114, p. 1123–1133, doi:10.5382/econgeo.4676.

Gopon, P., Singh, J., London, A., Hansen, L., Wade, J., and Moody, M., 2020, Extraction of S Isotopes from Geologic datasets, *in* Proceedings of the Field Emission Society special APT software meeting, p. 1, https://youtu.be/Cqi8_aurYrw.

Haase, C.S., Chadman, J., Feinn, D., and Ortoleva, P., 1980, Oscillatory Zoning in Plagioclase Feldspar: Science, v. 209, p. 272 LP – 274, doi:10.1126/science.209.4453.272.

Haley, D., Choi, P., and Raabe, D., 2015, Guided mass spectrum labelling in atom probe tomography.: Ultramicroscopy, v. 159 Pt 2, p. 338–45, doi:10.1016/j.ultramic.2015.03.005.

678 Halliday, A.N., and Lee, D.C., 1999, Tungsten isotopes and the early development of the Earth
679 and Moon: Geochimica et Cosmochimica Acta, v. 63, p. 4157–4179, doi:10.1016/s0016-
680 7037(99)00315-4.

681 Hauri, E.H., Papineau, D., Wang, J., and Hillion, F., 2016, High-precision analysis of multiple
682 sulfur isotopes using NanoSIMS: Chemical Geology, v. 420, p. 148–161,
683 doi:10.1016/j.chemgeo.2015.11.013.

684 Haycock, R., and Kingham, D.R., 1980, Post-ionization of Field-Evaporated Ions: Physics
685 Review Letters, v. 44, p. 1520–1523.

686 Hervig, R.L., Mazdab, F.K., Williams, P., Guan, Y., Huss, G.R., and Leshin, L.A., 2006, Useful
687 ion yields for Cameca IMS 3f and 6f SIMS: Limits on quantitative analysis: Chemical
688 Geology, v. 227, p. 83–99, doi:10.1016/j.chemgeo.2005.09.008.

689 Jensen, M.L., Nakai, N., 1962, Sulfur isotope meteorite standards results and recommendations,
690 *in* Biochemistry of Sulfur Isotopes, NSF Symposium, p. 30–35.

691 Kautz, E., Cliff, J., Lach, T., Reilly, D., and Devaraj, A., 2021, Correlating nanoscale secondary
692 ion mass spectrometry and atom probe tomography analysis of uranium enrichment in
693 metallic nuclear fuel: Analyst, v. 146, p. 69–74, doi:10.1039/d0an01831g.

694 Kelly, T.F., 2020, Project Tomo: in pursuit of Atomic-Scale Analytical Tomography, *in*
695 Proceedings of the Atom Probe Tomography and Microscopy Conference, p. 1.

696 De Laeter, J.R., Böhlke, J.K., De Bièvre, P., Hidaka, H., Peiser, H.S., Rosman, K.J.R., and
697 Taylor, P.D.P., 2003, Atomic weights of the elements: Review 2000 (IUPAC Technical
698 Report): Pure and Applied Chemistry, v. 75, p. 683–800, doi:10.1351/pac200375060683.

699 Larson, D.J., Prosa, T.J., Ulfig, R.M., Geiser, B.P., and Kelly, T.F., 1999, Local Electrode Atom
700 Probe Tomography: a user's guide: New York, Springer, 328 p., doi:10.1007/978-1-4614-
701 8721-0.

702 London, A.J., 2019, Quantifying Uncertainty from Mass-Peak Overlaps in Atom Probe
703 Microscopy: Microscopy and Microanalysis, v. early onli, p. 1–11,
704 doi:10.1017/S1431927618016276.

705 McKeegan, K.D., and Leshinv, L.A., 2001, Chapter 4. Stable Isotope Variations in
706 Extraterrestrial Materials, *in* Valley, J.W. and Cole, D.R. eds., Reviews in Mineralogy and
707 Geochemistry, Vol. 43, Stable Isotope Geochemistry, p. 279–318.

708 Meija, J. et al., 2016, Isotopic compositions of the elements 2013 (IUPAC Technical Report):
709 Pure and Applied Chemistry, v. 88, p. 293–306, doi:10.1515/pac-2015-0503.

710 Meisenkothen, F., Mclean, M., Kalish, I., Samarov, D. V., and Steel, E.B., 2020a, Atom Probe
711 Mass Spectrometry of Uranium Isotopic Reference Materials: Analytical Chemistry, v. 92,
712 p. 11388–11395, doi:10.1021/acs.analchem.0c02273.

713 Meisenkothen, F., McLean, M., Kalish, I., Samarov, D., and Steel, E., 2020b, Towards Accurate
714 and Reproducible Uranium Isotopic Analysis via Atom Probe Mass Spectrometry:
715 Microscopy and Microanalysis, v. 26, p. 176–177, doi:10.1017/s1431927620013689.

716 Meisenkothen, F., Samarov, D. V., Kalish, I., and Steel, E.B., 2020c, Exploring the accuracy of
717 isotopic analyses in atom probe mass spectrometry: Ultramicroscopy, v. 216, p. 113018,
718 doi:10.1016/j.ultramic.2020.113018.

719 Meisenkothen, F., Steel, E.B., Prosa, T.J., Henry, K.T., and Prakash Kolli, R., 2015, Effects of

detector dead-time on quantitative analyses involving boron and multi-hit detection events in atom probe tomography: Ultramicroscopy, v. 159, p. 101–111, doi:10.1016/j.ultramic.2015.07.009.

Nesse, W., 2000, Introduction to Mineralogy: New York, Oxford Univerity Press, 442 p.

Peterman, E.M., Reddy, S.M., Saxey, D.W., Snoeyenbos, D.R., Rickard, W.D.A., Fougerouse, D., and Kylander-clark, A.R.C., 2016, Nanogeochronology of discordant zircon measured by atom probe microscopy of Pb-enriched dislocation loops: Science Advances, v. 2, p. 1–9, doi:10.1126/sciadv.1601318.

Prosa, T.J., and Oltman, E., 2021, Study of LEAP 5000 Deadtime and Precision via Silicon Pre-Sharpened-Microtip Standard Specimens, *in* Microscopy and Microanalysis, p. 1.

Prosa, T.J., Reinhard, D.A., Saint-Cyr, H.F., Martin, I., Rice, K.P., Yimeng, C., and Larson, D.J., 2017, Evolution of Atom Probe Data Collection Toward Optimized and Fully Automated Acquisition: Microscopy and Microanalysis, v. 23(S1), p. 616–617.

Saxey, D.W., 2011, Correlated ion analysis and the interpretation of atom probe mass spectra: Ultramicroscopy, v. 111, p. 473–479, doi:10.1016/j.ultramic.2010.11.021.

Schertl, H.-P., Maresch, W. V., Stanek, K.P., Hertwig, A., Krebs, M., Baese, R., and Sergeev, S.S., 2012, New occurrences of jadeitite, jadeite quartzite and jadeite-lawsonite quartzite in the Dominican Republic, Hispaniola: petrological and geochronological overview: European Journal of Mineralogy, v. 24, p. 199–216, doi:10.1127/0935-1221/2012/0024-2201.

Seydoux-Guillaume, A.-M., Fougerouse, D., Laurent, A.-T., Gardés, E., Reddy, S.M., and

741 Saxey, D.W., 2018, Nanoscale resetting of the Th/Pb system in an isotopically-closed
742 monazite grain: a combined atom probe and transmission electron microscopy study:
743 Geoscience Frontiers, doi:10.1016/j.gsf.2018.09.004.

744 Spero, H.J., Bijma, J., Lea, D.W., and Bernis, B.E., 1997, Effect of seawater carbonate
745 concentration on foraminiferal carbon and oxygen isotopes: Nature, v. 390, p. 497–500,
746 doi:10.1038/37333.

747 Tanner, D., Henley, R.W., Mavrogenes, J.A., and Holden, P., 2016, Sulfur isotope and trace
748 element systematics of zoned pyrite crystals from the El Indio Au–Cu–Ag deposit, Chile:
749 Contributions to Mineralogy and Petrology, v. 171, p. 1–17, doi:10.1007/s00410-016-1248-
750 6.

751 Thompson, K., Lawrence, D., Larson, D.J., Olson, J.D., Kelly, T.F., and Gorman, B., 2007, In
752 situ site-specific specimen preparation for atom probe tomography: Ultramicroscopy, v.
753 107, p. 131–139, doi:10.1016/j.ultramic.2006.06.008.

754 Thuvander, M., J. Weidow, J., Angseryd, J., Falk, L.K.L.L., Liu, F., Sonestedt, M., Stiller, K.,
755 Andrén, H.O., and Andr??n, H.O., 2011, Quantitative atom probe analysis of carbides:
756 Ultramicroscopy, v. 111, p. 604–608, doi:10.1016/j.ultramic.2010.12.024.

757 Thuvander, M., Shinde, D., Rehan, A., Ejnermark, S., and Stiller, K., 2019, Improving
758 Compositional Accuracy in APT Analysis of Carbides Using a Decreased Detection
759 Efficiency: Microscopy and Microanalysis, v. 25, p. 454–461,
760 doi:10.1017/S1431927619000424.

761 Valley, J.W. et al., 2014, Hadean age for a post-magma-ocean zircon confirmed by atom-probe
762 tomography: Nature Geoscience, v. 7, p. 219–223, doi:10.1038/ngeo2075.

763 Valley, J.W., Reinhard, D.A., Cavosie, A.J., Ushikubo, T., Lawrence, D.F., Larson, D.J., Kelly,
764 T.F., Snoeyenbos, D.R., and Strickland, A., 2015, Presidential Address. Nano-and micro-
765 geochronology in Hadean and Archean zircons by atom-probe tomography and SIMS: New
766 tools for old minerals: American Mineralogist, v. 100, p. 1355–1377, doi:10.2138/am-2015-
767 5134.

768 Walters, J.B., Cruz-Uribe, A.M., and Marschall, H.R., 2019, Isotopic compositions of sulfides in
769 exhumed high-pressure terranes: Implications for sulfur cycling in subduction zones:
770 Geochemistry, Geophysics, Geosystems, p. 2019GC008374, doi:10.1029/2019GC008374.

771

772

Figures and Supplementary Materials for

Atom probe tomography for isotopic analysis: development of the $^{34}S/^{32}S$ system in sulfides

Phillip Gopon, James O. Douglas, Frederick Meisenkothen, Jaspreet Singh, Andrew London, Michael P. Moody

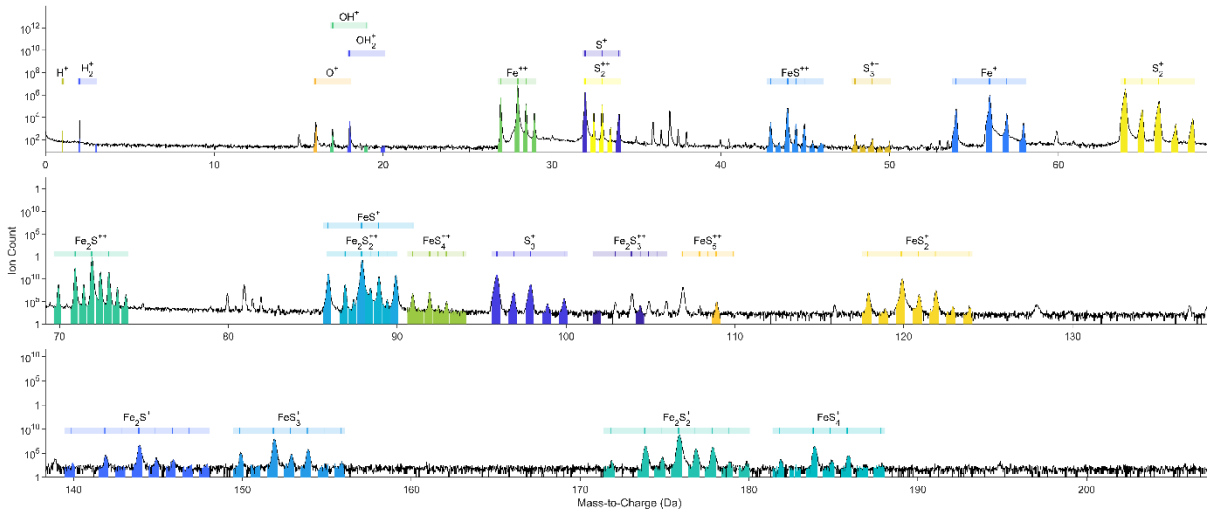

Figure 1: Mass spectrum of dataset R5083_08493, showing the complexity of the mass spectrum as well as the overlaps present on the main S peak family (34 Da, 33 Da, 34 Da, and 36 Da). Note only the main peaks are labeled for sake of clarity.

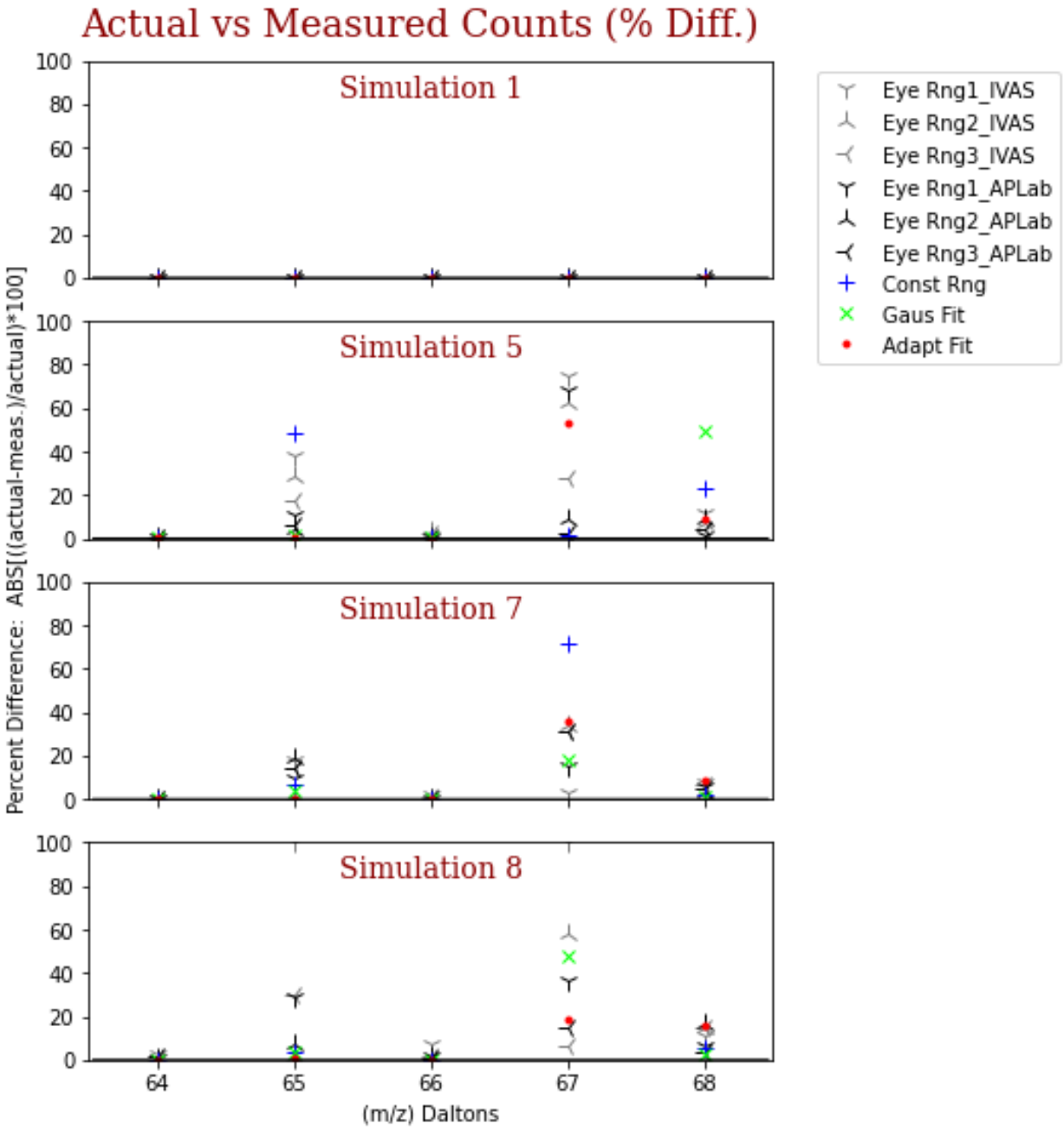

784

785 Figure 2: Plot of the deviation of the various methods of peak count determination from the 'actual.' Note values

786 shown are absolute values of percent differences calculated from the values in Table 1.

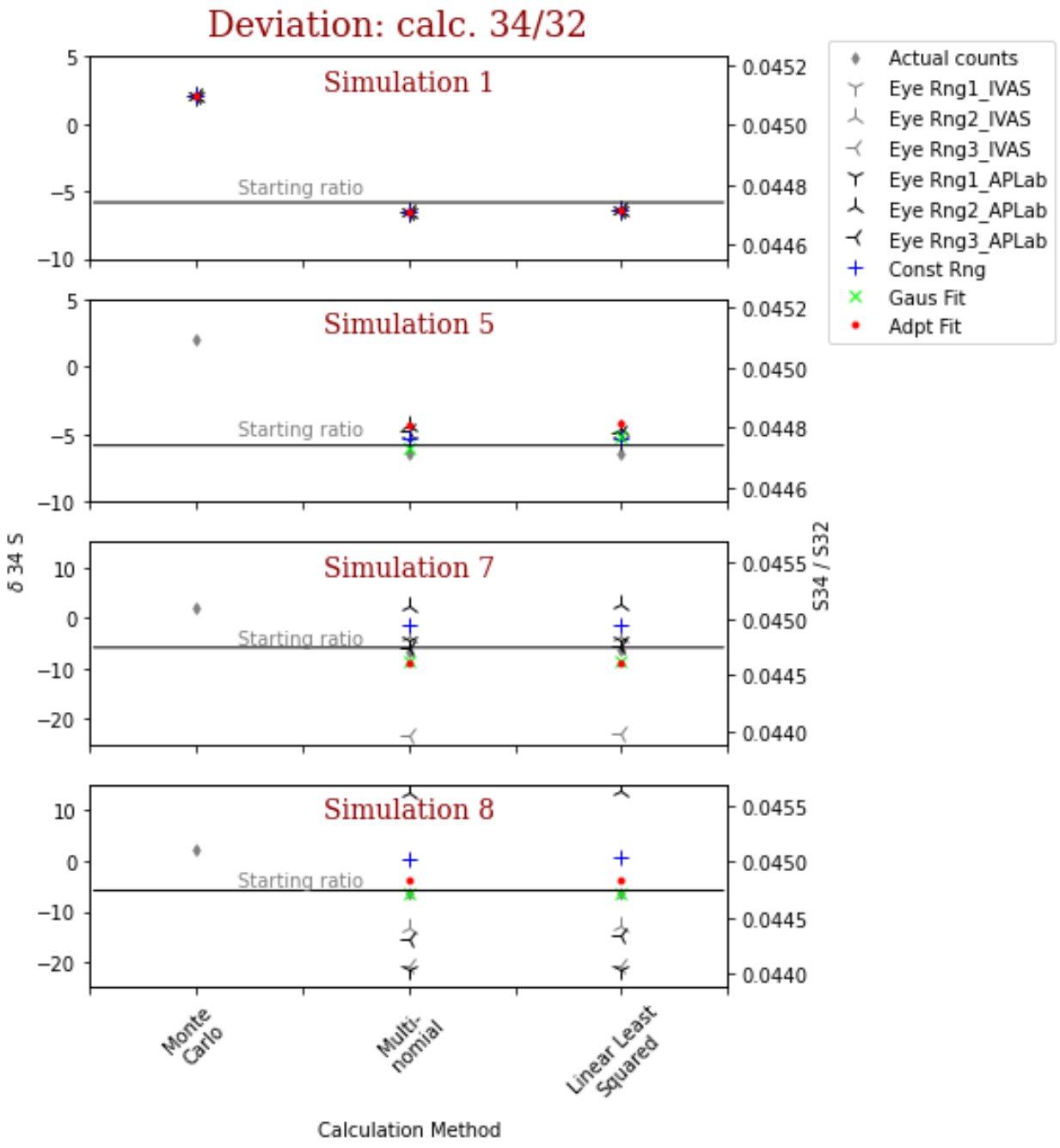

787

788 Figure 3: Comparison of three different methods to determine the $^{34}S/^{32}S$ ratios (from Table 1). Plotted as both
789 $\delta^{34}S$ (left axis) and absolute $^{34}S/^{32}S$ ratio (right axis). Note that only ± 20 ‰ $\delta^{34}S$ is shown. Values outside of this
790 range can be found in Table 1. With the exception of Simulation 1, all calculations using the Monte Carlo
791 Approach are outside of this range.

792

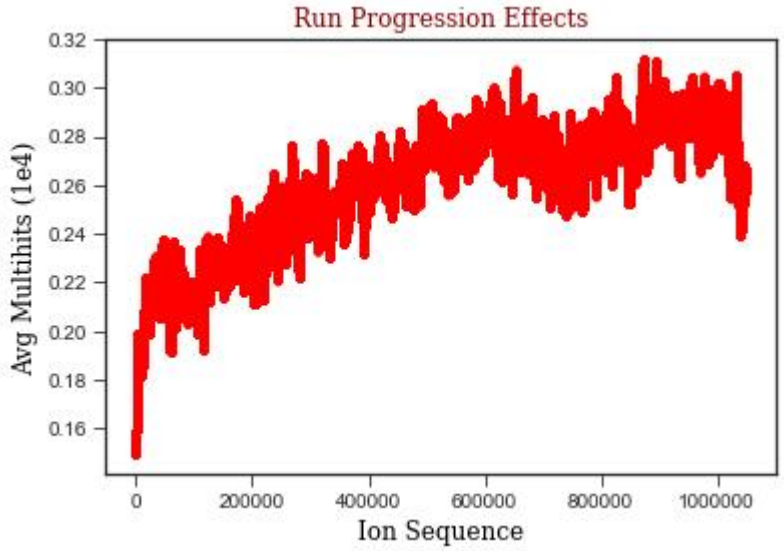

Figure 4: The ion hit sequence plotted versus multi-hits (averaged over $1e^4$ ion hits) for dataset R5083_08493. Note the increase in multi-hits as the run progresses.

799

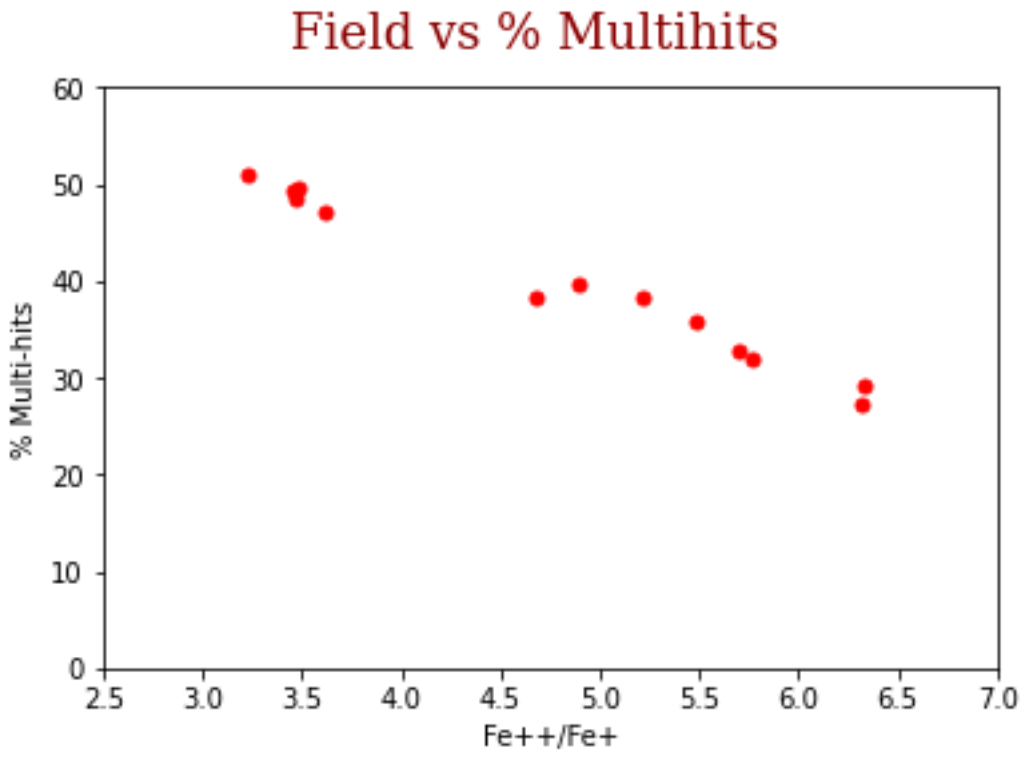

800

801 Figure 5: Plot of % multi-hits versus the charge state ratio of Fe^{++}/Fe^{+} (from Table 2). The CSR is used here as a
802 direct proxy for the local electric field.

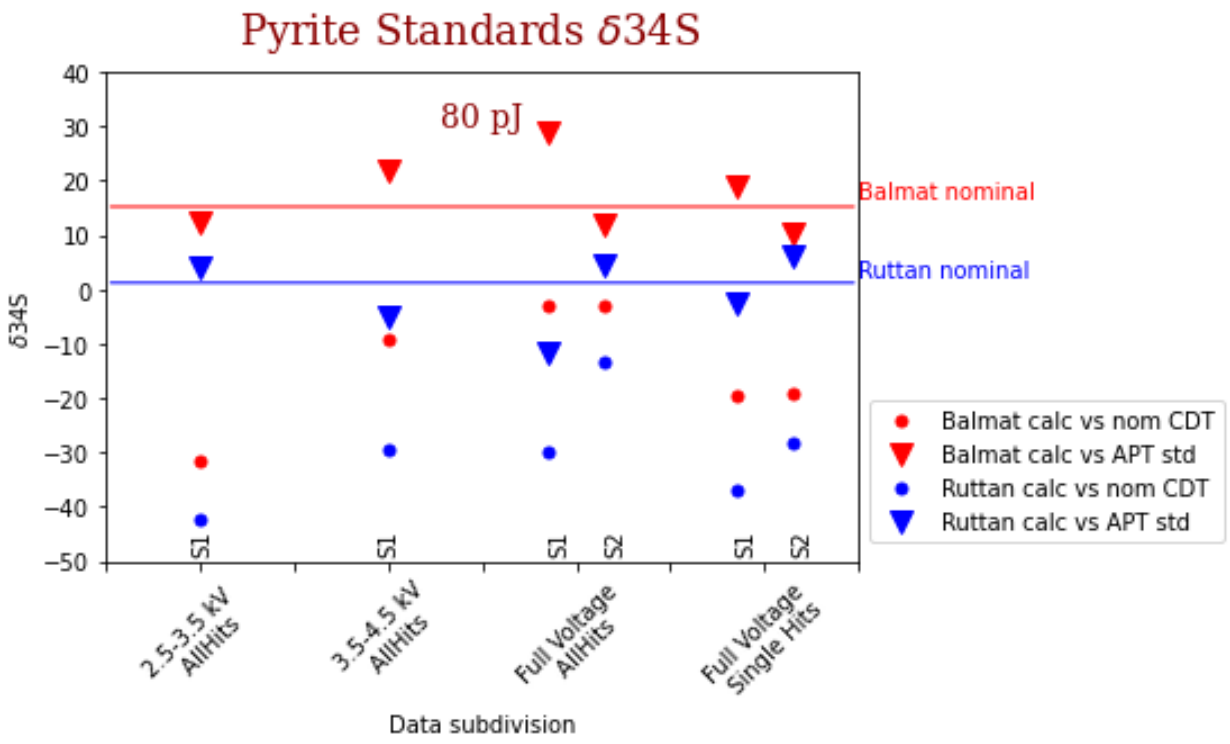

Figure 6: Comparison of calculated $\delta^{34}S$ of datasets of pyrite standards run at 80 pJ. Data is subdivided by specific voltage ranges, as well as if only single hits or all hits are used. S1 means dataset pair 08492/08493 and S2 dataset pair 11434/11435. Data is shown both calculated against the nominal CDT value (Equation 8) and against a known standard (Equation 9).

				Intensities Normalized to 1					d34S	d34S	d34S	d34S
Starting' d34S =	-5.84			64 counts	65 counts	66 counts	67 counts	68 counts	Monte Carlo	Multinomial	Linear L.S.	Actual
Simulation	Peak cnt method		Bkg method									
Sim 1	*Actual*		*none need*	0.902318	0.014295	0.080746	0.000649	0.001993	2.05	-6.50	-6.39	-5.84
		1	*IVAS*	0.902318	0.014295	0.080746	0.000649	0.001993	2.05	-6.50	-6.39	-5.84
		1	*APT Lab*	0.902318	0.014295	0.080746	0.000649	0.001993	2.05	-6.50	-6.39	-5.84
	Eye Rangir	*2*	*IVAS*	0.902318	0.014295	0.080746	0.000649	0.001993	2.05	-6.50	-6.39	-5.84
		2	*APT Lab*	0.902318	0.014295	0.080746	0.000649	0.001993	2.05	-6.50	-6.39	-5.84
		3	*IVAS*	0.902318	0.014295	0.080746	0.000649	0.001993	2.05	-6.50	-6.39	-5.84
		3	*APT Lab*	0.902318	0.014295	0.080746	0.000649	0.001993	2.05	-6.50	-6.39	-5.84
	Constant Range		*IVAS*	0.902318	0.014295	0.080746	0.000649	0.001993	2.05	-6.50	-6.39	-5.84
	Gaussian Fit (FWHM)		*linear*									
	Adapt. pk fit		*constant*	0.902318	0.014295	0.080746	0.000649	0.001992	2.05	-6.50	-6.39	-5.84
Sim 5	*Actual*		*none need*	0.902241	0.014246	0.080888	0.000637	0.001988	-6.99	-4.56	-4.56	-5.84
		1	*IVAS*	0.909896	0.008771	0.079416	0.000159	0.001758	-374.50	-30.58	-30.58	-5.84
		1	*APT Lab*	0.904224	0.012633	0.080984	0.000202	0.001957	-405.15	-5.51	-5.45	-5.84
	Eye Rangir	*2*	*IVAS*	0.896353	0.018281	0.083278	0.000241	0.001847	-450.54	31.05	30.93	-5.84
		2	*APT Lab*	0.902948	0.013682	0.080968	0.000583	0.001819	-30.12	-4.39	-4.56	-5.84
		3	*IVAS*	0.899317	0.011750	0.082903	0.000462	0.005567	-54.31	23.70	25.94	-5.84
		3	*APT Lab*	0.902915	0.013428	0.080938	0.000652	0.002067	35.44	-4.71	-4.97	-5.84
	Constant Range		*APT Lab*	0.909017	0.007384	0.081416	0.000646	0.001538	-35.42	-5.26	-5.26	-5.84
	Gaussian Fit (FWHM)		*linear*	0.899611	0.014020	0.080536	0.002865	0.002968	498.87	-6.07	-5.14	-5.84
	Adapt. pk fit		*constant*	0.901776	0.014219	0.080868	0.000976	0.002161	138.28	-4.39	-4.16	-5.84
Sim 7	*Actual*		*none need*	0.902460	0.014241	0.080673	0.000634	0.001993	-9.24	-7.54	-7.44	-5.84
		1	*IVAS*	0.907144	0.011612	0.078783	0.000615	0.001846	25.22	-35.58	-35.50	-5.84
		1	*APT Lab*	0.901137	0.015628	0.080816	0.000540	0.001880	-125.67	-4.46	-4.44	-5.84
	Eye Rangir	*2*	*IVAS*	0.901757	0.014547	0.080936	0.000848	0.001912	51.43	-3.56	-3.49	-5.84
		2	*APT Lab*	0.898424	0.016973	0.081144	0.001403	0.002055	128.74	2.45	2.65	-5.84
		3	*IVAS*	0.905754	0.012250	0.079690	0.000439	0.001867	-117.74	-23.02	-22.97	-5.84
		3	*APT Lab*	0.900747	0.016228	0.080688	0.000433	0.001904	-250.04	-5.77	-5.65	-5.84
	Constant Range		*APT Lab*	0.900630	0.015232	0.081010	0.001087	0.002040	109.90	-1.47	-1.31	-5.84
	Gaussian Fit (FWHM)		*linear*	0.901866	0.014815	0.080547	0.000750	0.002023	56.23	-8.50	-8.37	-5.84
	Adapt. pk fit		*constant*	0.902954	0.014207	0.080616	0.000406	0.001818	-206.51	-8.78	-8.79	-5.84
Sim 8	*Actual*		*none need*	0.902231	0.014208	0.080908	0.000650	0.002003	5.92	-4.39	-4.28	-5.84
		1	*IVAS*	0.923023	0.000000	0.075205	0.000000	0.001772	6026.58	-94.79	-94.67	-5.84
		1	*APT Lab*	0.899390	0.018292	0.079301	0.000886	0.002131	26.93	-21.56	-21.34	-5.84
	Eye Rangir	*2*	*IVAS*	0.902490	0.013977	0.080214	0.001025	0.002294	186.90	-13.20	-12.88	-5.84
		2	*APT Lab*	0.897537	0.015237	0.081935	0.002959	0.002333	305.70	13.42	13.97	-5.84
		3	*IVAS*	0.899880	0.018396	0.079418	0.000607	0.001699	-153.34	-20.66	-20.71	-5.84
		3	*APT Lab*	0.917043	-0.001202	0.081329	0.000747	0.002083	52.35	-15.42	-14.52	-5.84
	Constant Range		*APT Lab*	0.899972	0.014690	0.081083	0.002134	0.002122	207.92	0.22	0.56	-5.84
	Gaussian Fit (FWHM)		*linear*	0.902500	0.013727	0.080761	0.000960	0.002052	109.90	-6.45	-6.28	-5.84
	Adapt. pk fit		*constant*	0.902706	0.014085	0.080993	0.000528	0.001688	-91.25	-3.86	-3.94	-5.84

Table 1: Collation of various methods used to measure peak counts and to calculate the $^{34}S/^{32}S$ ratio. To save space, only Simulations 1,5,7,8 are shown. Results for all simulations are reported in Appendix C.

						Standard	Mineral		Formula	$^{34}S/^{32}S$	$\delta^{34}S$ (CDT)	
Canyon Diablo Troilite						Canyon Diablo	Troilite		FeS	0.045005	0	
Ruttan Pyrite						Ruttan	Pyrite		FeS2	0.045059	1.2	
Balmat Pyrite						Balmat	Pyrite		FeS2	0.045684	15.1	

80 pJ, Varying Ion Ratio	Ions e6	Instrument	Standard	Cond.	Dataset	Voltage Range	Fe^{++}/Fe^{+}	% Multihits	Data type	$^{34}S/^{32}S$	$\delta^{34}S$ (model CDT)	$\delta^{34}S$ (APT Stand)
Balmat_XR_8493_80pJ_2500-3500V_allHits	61	LEAP 5000-XR	Balmat	80pJ	08493	2500-3500V	6.33	29.19	all hits	0.043578	-32	12
Balmat_XR_8493_80pJ_3500_4500V_allHits	61	LEAP 5000-XR	Balmat	80pJ	08493	3500-4500V	5.49	35.89	all hits	0.044582	-9	22
Balmat_XR_8493_80pJ_fullvoltage_allHits	61	LEAP 5000-XR	Balmat	80pJ	08493	Full voltage	5.21	38.43	all hits	0.044872	-3	29
Balmat_XR_8493_80pJ_fullvoltage_singleHits		LEAP 5000-XR	Balmat	80pJ	08493	Full voltage			single hits	0.044118	-20	19
Balmat_XR_11434_80pJ_fullvoltage_allHits		LEAP 5000-XR	Balmat	80pJ	11434	Full voltage	4.89	39.69	all hits	0.044871	-3	12
Balmat_XR_11434_80pJ_fullvoltage_singleHits		LEAP 5000-XR	Balmat	80pJ	11434	Full voltage			single hits	0.044134	-19	10
Ruttan_XR_8492_80pJ_2500-3500V_allHits	25	LEAP 5000-XR	Ruttan	80pJ	08492	2500-3500V	6.32	27.29	all hits	0.043099	-42	4
Ruttan_XR_8492_80pJ_3500-4500V_allHits	25	LEAP 5000-XR	Ruttan	80pJ	08492	3500-4500V	5.7	32.81	all hits	0.043684	-29	-5
Ruttan_XR_8492_80pJ_fullvoltage_allHits	25	LEAP 5000-XR	Ruttan	80pJ	08492	Full Voltage	5.77	32.06	all hits	0.043665	-30	-12
Ruttan_XR_8492_80pJ_fullvoltage_singleHits		LEAP 5000-XR	Ruttan	80pJ	08492	Full Voltage			single hits	0.043341	-37	-2
Ruttan_XR_11435_80pJ_fullvoltage_allHits		LEAP 5000-XR	Ruttan	80pJ	11435	Full Voltage	4.68	38.23	all hits	0.044395	-14	4
Ruttan_XR_11435_80pJ_fullvoltage_singleHits		LEAP 5000-XR	Ruttan	80pJ	11435	Full Voltage			single hits	0.043732	-28	6
40 pJ, Varying Ion Ratio												
Balmat_XR_8462_40pJ_full_voltage_allHits	33	LEAP 5000-XR	Balmat	40pJ	08462	Full Voltage	3.23	51.09	all hits	0.045822	18	15
Balmat_XR_8462_40pJ_fullvoltage_singleHits		LEAP 5000-XR	Balmat	40pJ	08462	Full Voltage			single hits	0.044802	-5	17
Balmat_XR_8460_40pJ_fullvoltage_allHits	20	LEAP 5000-XR	Balmat	40pJ	08460	Full Voltage	3.48	49.73	all hits	0.045561	12	9
Balmat_XR_8460_40pJ_fullvoltage_singleHits		LEAP 5000-XR	Balmat	40pJ	08460	Full Voltage			single hits	0.044549	-10	11
Ruttan_XR_8458_40pJ_fullvoltage_allHits	16	LEAP 5000-XR	Ruttan	40pJ	08458	Full Voltage	3.47	48.54	all hits	0.045188	4	1
Ruttan_XR_8458_40pJ_fullvoltage_singleHits		LEAP 5000-XR	Ruttan	40pJ	08458	Full Voltage			single hits	0.044121	-20	0
80 pJ, Constant Ion Ratio, $^{32}S^{1+}/^{32,32}S_2^{1+}$ = 1:1												
Balmat_XR_9023_fullvoltage_allHits	26	LEAP 5000-XR	Balmat	S^{+}/S_2^{+}=1:1	09023	Full Voltage	3.46	49.23	all hits	0.045829	18	22
Balmat_XR_9023_fullvoltage_singleHits		LEAP 5000-XR	Balmat	S^{+}/S_2^{+}=1:1	09023	Full Voltage			single hits	0.044806	-4	24
Ruttan_XR_9021_fullvoltage_allHits	20	LEAP 5000-XR	Ruttan	S+/S2+=1:1	09021	Full Voltage	3.62	47.1	all hits	0.044894	-2	-5
Ruttan_XR_9021_fullvoltage_singleHits		LEAP 5000-XR	Ruttan	S+/S2+=1:1	09021	Full Voltage			single hits	0.043822	-26	-7

Table 2: Run conditions, calculated $^{34}S/^{32}S$, and $\delta^{34}S$ for each dataset and subdivision of each dataset. Multi-hit fractions as well as the corresponding Fe^{++}/Fe^{+} ratio (as a proxy for the local field), were calculated for the data containing all hits. $\delta^{34}S$ is calculated both against the nominal CDT value (equation (8)) and calculated against the corresponding standard that was acquired closest in time (equation (9)). Note - other than applied voltage, all other acquisition conditions kept constant (see section 2).

Appendix A: Detailed table of all ranges used for the ranging exercise.

Analyst #	Sim. #	64 Da		65 Da		66 Da		67 Da	
		Start	End	Start	End	Start	End	Start	End
User 1	1	63.8440	64.1440	64.8440	65.1440	65.8400	66.1400	66.8390	67.1390
User 2	1	63.5510	64.3330	64.5520	65.3340	65.5500	66.3320	66.5440	67.3260
User 3	1	63.9160	63.9730	64.9250	64.9610	65.9130	65.9680	66.9180	66.9610
User 1	2	63.9350	63.9540	64.9390	64.9520	65.9270	65.9510	66.9240	66.9520
User 2	2	63.5510	64.3330	64.5520	65.3340	65.5500	66.3320	66.5440	67.3260
User 3	2	63.9200	63.9730	64.9250	64.9610	65.9130	65.9680	66.9180	66.9610
User 1	3	63.5580	64.3470	64.6080	65.3100	65.5780	66.3360	66.6460	67.2310
User 2	3	63.5510	64.3330	64.5520	65.3340	65.5500	66.3320	66.5440	67.3260
User 3	3	63.4920	64.3640	64.5570	65.3430	65.5450	66.3820	66.5980	67.3450
User 1	4	63.6090	64.2890	64.7040	65.2060	65.6590	66.2450	66.7030	67.1460
User 2	4	63.5650	64.3040	64.5890	65.2550	65.5210	66.2670	66.6140	67.2420
User 3	4	63.4740	64.3500	64.6350	65.2820	65.5870	66.3160	66.7130	67.1660
User 1	5	63.1760	64.5910	64.6270	65.3560	65.4010	66.5960	66.7500	67.1510
User 2	5	63.2990	64.5500	64.5500	65.3440	65.3540	66.5050	66.6840	67.2790
User 3	5	63.0550	64.5830	64.5990	65.3420	65.3690	66.5410	66.6040	67.3400
User 1	6	63.8550	64.8050	64.8790	65.8200	65.8640	66.8260	66.8930	67.7270
User 2	6	63.6590	64.2340	64.6570	65.2320	65.7720	66.3470	66.6540	67.2290
User 3	6	63.7920	64.8140	64.8430	65.7600	65.7890	66.8020	66.8380	67.7020
User 1	7	63.8670	64.8500	64.8880	65.6280	65.8680	66.8610	66.8850	67.0550
User 2	7	63.6590	64.2340	64.6570	65.2320	65.6610	66.2360	66.6540	67.2290
User 3	7	63.7790	64.8130	64.8550	65.7790	65.8380	66.6850	66.8380	67.0750
User 1	8	63.7520	64.8380	64.8570	65.7930	65.8230	66.8010	66.8270	67.2140
User 2	8	63.6590	64.2340	64.6570	65.2320	65.6610	66.2360	66.6540	67.2290
User 3	8	63.6770	64.7850	64.7930	65.6400	65.7350	66.6850	66.8200	67.0580

Appendix B: Simulated spectra (Simulations 1-8)

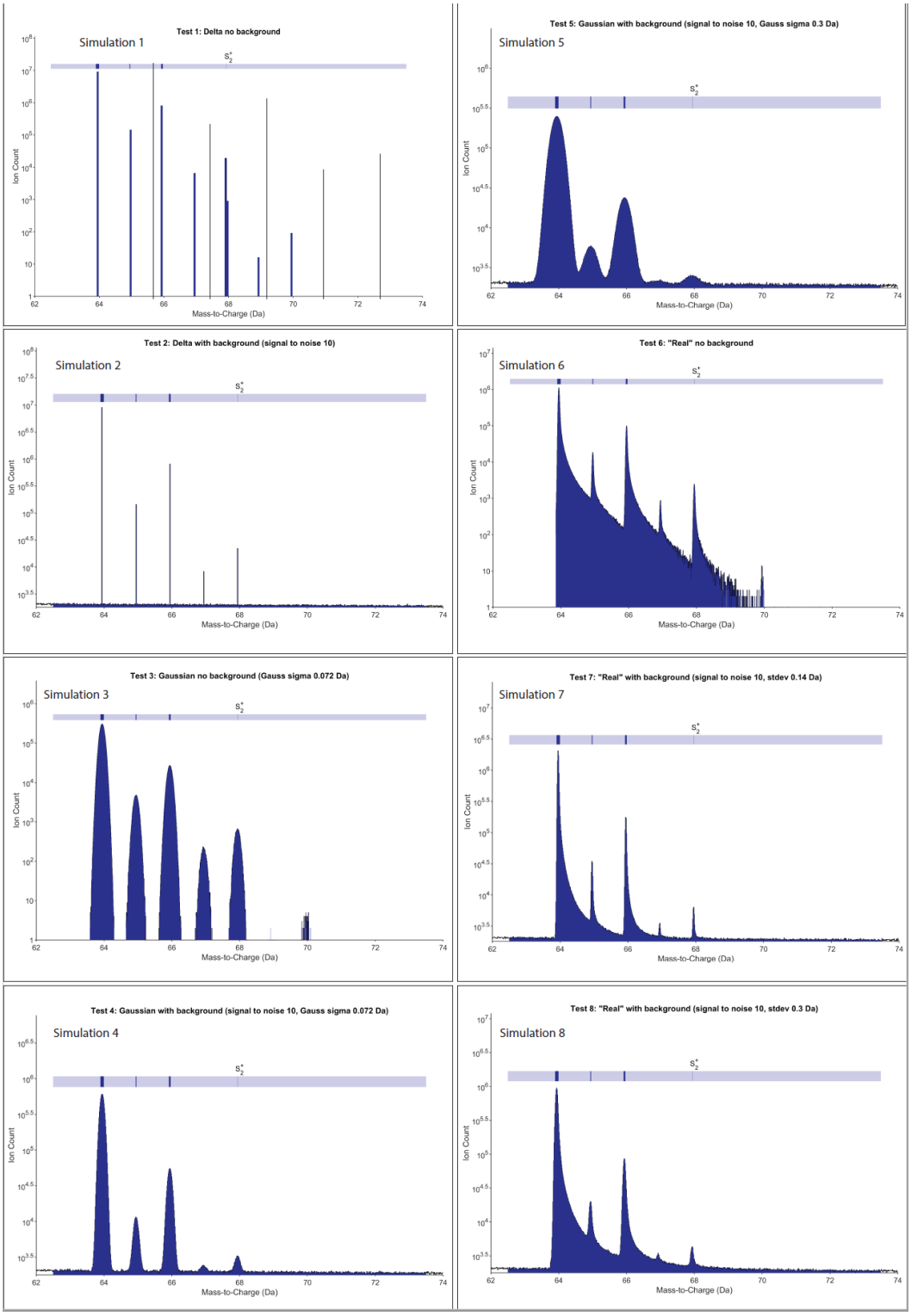

Appendix C: Full simulated data results (Simulations 1-8)

			normalized to 1					d34S	d34S	d34S	d34S
			64 counts	65 counts	66 counts	67 counts	68 counts	Monte Carlo	Multinomial	Linear Lst. Sqr.	Actual
Simulation	Peak cnt method	Bkg method									
Sim 1	*Actual*	*none need*	0.902318	0.014295	0.080746	0.000649	0.001993	2.05	-6.50	-6.39	-5.84
	1	*IVAS*	0.902318	0.014295	0.080746	0.000649	0.001993	2.05	-6.50	-6.39	-5.84
	1	*APT Lab*	0.902318	0.014295	0.080746	0.000649	0.001993	2.05	-6.50	-6.39	-5.84
	Eye Rangir	*2 IVAS*	0.902318	0.014295	0.080746	0.000649	0.001993	2.05	-6.50	-6.39	-5.84
	2	*APT Lab*	0.902318	0.014295	0.080746	0.000649	0.001993	2.05	-6.50	-6.39	-5.84
	3	*IVAS*	0.902318	0.014295	0.080746	0.000649	0.001993	2.05	-6.50	-6.39	-5.84
	3	*APT Lab*	0.902318	0.014295	0.080746	0.000649	0.001993	2.05	-6.50	-6.39	-5.84
	Constant Range	*IVAS*	0.902318	0.014295	0.080746	0.000649	0.001993	2.05	-6.50	-6.39	-5.84
	Gaussian Fit (FWHM)	*linear*									
	Adapt. pk fit	*constant*	0.902318	0.014295	0.080746	0.000649	0.001992	2.05	-6.50	-6.39	-5.84
Sim 2	*Actual*	*none need*	0.902422	0.014211	0.080738	0.000625	0.002005	-15.39	-6.69	-6.58	-5.84
	1	*IVAS*	0.902408	0.014210	0.080731	0.000639	0.002012	-4.75	-6.77	-6.65	-5.84
	1	*APT Lab*	0.902404	0.014213	0.080739	0.000635	0.002009	-8.50	-6.67	-6.55	-5.84
	Eye Rangir	*2 IVAS*	0.902524	0.014143	0.080741	0.000591	0.002001	-38.27	-6.76	-6.66	-5.84
	2	*APT Lab*	0.902448	0.014175	0.080744	0.000627	0.002006	-10.86	-6.65	-6.54	-5.84
	3	*IVAS*	0.902400	0.014221	0.080727	0.000638	0.002014	-4.75	-6.81	-6.70	-5.84
	3	*APT Lab*	0.902410	0.014218	0.080727	0.000634	0.002011	-7.77	-6.82	-6.71	-5.84
	Constant Range	*APT Lab*	0.902482	0.014191	0.080716	0.000631	0.001980	-9.39	-7.03	-6.93	-5.84
	Gaussian Fit (FWHM)	*linear*									
	Adapt. pk fit	*constant*	0.902421	0.014209	0.080738	0.000625	0.002007	-15.42	-6.70	-6.58	-5.84
Sim 3	*Actual*	*none need*	0.902088	0.014277	0.080980	0.000647	0.002007	0.58	-3.25	-3.25	-5.84
	1	*IVAS*	0.902088	0.014277	0.080980	0.000647	0.002007	0.58	-3.36	-3.25	-5.84
	1	*APT Lab*	0.902088	0.014277	0.080980	0.000647	0.002007	0.58	-3.36	-3.25	-5.84
	Eye Rangir	*2 IVAS*	0.902088	0.014277	0.080980	0.000647	0.002007	0.58	-3.36	-3.25	-5.84
	2	*APT Lab*	0.902088	0.014277	0.080980	0.000647	0.002007	0.58	-3.36	-3.25	-5.84
	3	*IVAS*	0.902088	0.014277	0.080980	0.000647	0.002007	0.58	-3.36	-3.25	-5.84
	3	*APT Lab*	0.902088	0.014277	0.080980	0.000647	0.002007	0.58	-3.36	-3.25	-5.84
	Constant Range	*APT Lab*	0.902117	0.014279	0.080987	0.000630	0.001987	-11.55	-3.20	-3.20	-5.84
	Gaussian Fit (FWHM)	*linear*	0.902025	0.014170	0.081122	0.000713	0.001970	49.80	-1.53	-1.44	-5.84
	Adapt. pk fit	*constant*	0.902080	0.014267	0.080996	0.000644	0.002012	-0.93	-3.14	-3.04	-5.84
Sim 4	*Actual*	*none need*	0.902446	0.014211	0.080714	0.000638	0.001991	-4.80	-6.92	-6.92	-5.84
	1	*IVAS*	0.902193	0.014116	0.080870	0.000884	0.001937	65.06	-4.81	-4.72	-5.84
	1	*APT Lab*	0.902445	0.014228	0.080727	0.000633	0.001968	-9.24	-6.86	-6.77	-5.84
	Eye Rangir	*2 IVAS*	0.902178	0.014191	0.080601	0.000611	0.002420	-27.15	-8.12	-7.77	-5.84
	2	*APT Lab*	0.902463	0.014226	0.080724	0.000624	0.001964	-16.81	-6.92	-6.83	-5.84
	3	*IVAS*	0.901436	0.015010	0.080618	0.000841	0.002096	100.59	-7.18	-6.99	-5.84
	3	*APT Lab*	0.902450	0.014245	0.080702	0.000629	0.001974	-11.55	-7.18	-7.09	-5.84
	Constant Range	*APT Lab*	0.902525	0.014235	0.080667	0.000638	0.001934	-6.28	-7.61	-7.61	-5.84
	Gaussian Fit (FWHM)	*linear*	0.901900	0.014230	0.080648	0.001088	0.002134	142.42	-7.24	-7.01	-5.84
	Adapt. pk fit	*constant*	0.902462	0.014203	0.080639	0.000686	0.002010	31.55	-7.97	-7.84	-5.84
Sim 5	Actual	none need	0.902240644	0.014245654	0.080887974	0.000637407	0.001988321	-6.99	-4.56	-4.56	-5.84
	1	IVAS	0.909896005	0.008771452	0.079415592	0.000158689	0.001758262	-374.50	-30.58	-30.58	-5.84
	1	APT Lab	0.904223641	0.012632921	0.080984269	0.000202283	0.001956886	-405.15	-5.51	-5.45	-5.84
	Eye Rangir	2 IVAS	0.896352719	0.018280659	0.083277856	0.000241392	0.001847374	-450.54	31.05	30.93	-5.84
	2	APT Lab	0.902947924	0.013682173	0.080968127	0.000582662	0.001819114	-30.12	-4.39	-4.56	-5.84
	3	IVAS	0.899317377	0.011749941	0.082903092	0.000462345	0.005567246	-54.31	23.70	25.94	-5.84
	3	APT Lab	0.902915142	0.013427944	0.080937738	0.000652279	0.002066897	35.44	-4.71	-4.97	-5.84
	Constant Range	APT Lab	0.909017022	0.007383716	0.08141581	0.000645522	0.00153793	-35.42	-5.26	-5.26	-5.84
	Gaussian Fit (FWHM)	linear	0.899611134	0.014019648	0.080536226	0.00286533	0.002967663	498.87	-6.07	-5.14	-5.84
	Adapt. pk fit	constant	0.90177589	0.014218601	0.080868008	0.0009763	0.0021612	138.28	-4.39	-4.16	-5.84
Sim 6	Actual	none need	0.902257542	0.01432024	0.080775192	0.000630706	0.00201632	-11.55	-6.07	-5.95	-5.84
	1	IVAS	0.904698878	0.013849068	0.07958078	0	0.001871275	6026.58	-23.37	-23.36	-5.84
	1	APT Lab	0.902115099	0.014794896	0.080616698	0.000509313	0.001963994	-129.77	-7.91	-7.83	-5.84
	Eye Rangir	2 IVAS	0.90183008	0.013778033	0.081791287	0.00060253	0.001998069	-10.08	6.97	7.05	-5.84
	2	APT Lab	0.900050043	0.015481984	0.081631215	0.000824572	0.002012186	70.05	6.81	6.92	-5.84
	3	IVAS	0.904428247	0.011759052	0.081079572	0.000832052	0.001901077	64.29	-4.49	-4.42	-5.84
	3	APT Lab	0.901691875	0.01479123	0.080797228	0.000756773	0.001962893	52.22	-5.22	-5.13	-5.84
	Constant Range	APT Lab	0.901936679	0.01456112	0.080786913	0.000696181	0.002019107	27.64	-5.60	-5.47	-5.84
	Gaussian Fit (FWHM)	linear	0.902346545	0.01417704	0.080817475	0.000631945	0.002026995	-7.00	-5.63	-5.51	-5.84
	Adapt. pk fit	constant	0.9023554	0.0142861	0.0808003	0.0005821	0.0019761	-49.19	-5.86	-5.78	-5.84
Sim 7	Actual	none need	0.902459947	0.014240854	0.080672871	0.000633507	0.001992822	-9.24	-7.54	-7.44	-5.84
	1	IVAS	0.907144186	0.011611837	0.078783121	0.000614797	0.001846058	25.22	-35.58	-35.50	-5.84
	1	APT Lab	0.901136939	0.015627867	0.080816169	0.000539522	0.001879502	-125.67	-4.46	-4.44	-5.84
	Eye Rangir	2 IVAS	0.901757425	0.014547371	0.080935854	0.000847723	0.001911627	51.43	-3.56	-3.49	-5.84
	2	APT Lab	0.898424369	0.016973062	0.081144263	0.001402908	0.002055397	128.74	2.45	2.65	-5.84
	3	IVAS	0.905754204	0.012249865	0.079690481	0.000438719	0.001866731	-117.74	-23.02	-22.97	-5.84
	3	APT Lab	0.900746834	0.016228182	0.080688158	0.000433215	0.001903611	-250.04	-5.77	-5.65	-5.84
	Constant Range	APT Lab	0.900630342	0.015232457	0.081009779	0.00108739	0.002040033	109.90	-1.47	-1.31	-5.84
	Gaussian Fit (FWHM)	linear	0.901865823	0.014814727	0.080546895	0.000749661	0.002022894	56.23	-8.50	-8.37	-5.84
	Adapt. pk fit	constant	0.9029538	0.0142065	0.0806164	0.0004058	0.0018175	-206.51	-8.78	-8.79	-5.84
Sim 8	Actual	none need	0.902230583	0.014207948	0.080908341	0.000649907	0.002003221	5.92	-4.39	-4.28	-5.84
	1	IVAS	0.9230227	0	0.075205287	0	0.001772013	6026.58	-94.79	-94.67	-5.84
	1	APT Lab	0.899390327	0.018292039	0.079300768	0.000886182	0.002130684	26.93	-21.56	-21.34	-5.84
	Eye Rangir	2 IVAS	0.902490243	0.013976857	0.08021399	0.001025285	0.002293624	186.90	-13.20	-12.88	-5.84
	2	APT Lab	0.897536586	0.015236924	0.081934901	0.002959021	0.002332568	305.70	13.42	13.97	-5.84
	3	IVAS	0.899880424	0.018395772	0.07941766	0.000607485	0.00169866	-153.34	-20.66	-20.71	-5.84
	3	APT Lab	0.917042553	-0.001201579	0.081328999	0.000747022	0.002083005	52.35	-15.42	-14.52	-5.84
	Constant Range	APT Lab	0.899971558	0.014689764	0.081083317	0.00213386	0.002121501	207.92	0.22	0.56	-5.84
	Gaussian Fit (FWHM)	linear	0.902500133	0.013726744	0.080761235	0.000959539	0.002052348	109.90	-6.45	-6.28	-5.84
	Adapt. pk fit	constant	0.902706	0.014085	0.0809931	0.0005276	0.0016883	-91.25	-3.86	-3.94	-5.84

Appendix D: Full empirical data results (Adaptive fit, IVAS, and Gaussian)

Adaptive Peak Fitting

						Standard	Mineral		Formula	$^{34}S/^{32}S$	$\delta^{34}S$ (CDT)	
Canyon Diablo Troilite						**Canyon Diablo**	**Troilite**		**FeS**	**0.045005**	**0**	
Ruttan Pyrite						**Ruttan**	**Pyrite**		**FeS2**	**0.045059**	**1.2**	
Balmat Pyrite						**Balmat**	**Pyrite**		**FeS2**	**0.045684**	**15.1**	

80 pJ, Varying Ion Ratio	**Ions e6**	**Instrument**	**Standard**	**Cond.**	**Dataset**	**Voltage Range**	**Fe^{++}/Fe^{+}**	**% Multihits**	**Data type**	**$^{34}S/^{32}S$**	**$\delta^{34}S$ (model CDT)**	**$\delta^{34}S$ (APT Stand)**
Balmat_XR_8493_80pJ_2500-3500V_allHits	61	LEAP 5000-XR	Balmat	80pJ	08493	2500-3500V	6.33	29.19	all hits	0.043578	-32	12
Balmat_XR_8493_80pJ_3500_4500V_allHits	61	LEAP 5000-XR	Balmat	80pJ	08493	3500-4500V	5.49	35.89	all hits	0.044582	-9	22
Balmat_XR_8493_80pJ_fullvoltage_allHits	61	LEAP 5000-XR	Balmat	80pJ	08493	Full voltage	5.21	38.43	all hits	0.044872	-3	29
Balmat_XR_8493_80pJ_fullvoltage_singleHits		LEAP 5000-XR	Balmat	80pJ	08493	Full voltage			single hits	0.044118	-20	19
Balmat_XR_11434_80pJ_fullvoltage_allHits		LEAP 5000-XR	Balmat	80pJ	11434	Full voltage	4.89	39.69	all hits	0.044871	-3	12
Balmat_XR_11434_80pJ_fullvoltage_singleHits		LEAP 5000-XR	Balmat	80pJ	11434	Full voltage			single hits	0.044134	-19	10
Ruttan_XR_8492_80pJ_2500-3500V_allHits	25	LEAP 5000-XR	Ruttan	80pJ	08492	2500-3500V	6.32	27.29	all hits	0.043099	-42	4
Ruttan_XR_8492_80pJ_3500-4500V_allHits	25	LEAP 5000-XR	Ruttan	80pJ	08492	3500-4500V	5.7	32.81	all hits	0.043684	-29	-5
Ruttan_XR_8492_80pJ_fullvoltage_allHits	25	LEAP 5000-XR	Ruttan	80pJ	08492	Full Voltage	5.77	32.06	all hits	0.043665	-30	-12
Ruttan_XR_8492_80pJ_fullvoltage_singleHits		LEAP 5000-XR	Ruttan	80pJ	08492	Full Voltage			single hits	0.043341	-37	-2
Ruttan_XR_11435_80pJ_fullvoltage_allHits		LEAP 5000-XR	Ruttan	80pJ	11435	Full Voltage	4.68	38.23	all hits	0.044395	-14	4
Ruttan_XR_11435_80pJ_fullvoltage_singleHits		LEAP 5000-XR	Ruttan	80pJ	11435	Full Voltage			single hits	0.043732	-28	6
40 pJ, Varying Ion Ratio												
Balmat_XR_8462_40pJ_full_voltage_allHits	33	LEAP 5000-XR	Balmat	40pJ	08462	Full Voltage	3.23	51.09	all hits	0.045822	18	15
Balmat_XR_8462_40pJ_fullvoltage_singleHits		LEAP 5000-XR	Balmat	40pJ	08462	Full Voltage			single hits	0.044802	-5	17
Balmat_XR_8460_40pJ_fullvoltage_allHits	20	LEAP 5000-XR	Balmat	40pJ	08460	Full Voltage	3.48	49.73	all hits	0.045561	12	9
Balmat_XR_8460_40pJ_fullvoltage_singleHits		LEAP 5000-XR	Balmat	40pJ	08460	Full Voltage			single hits	0.044549	-10	11
Ruttan_XR_8458_40pJ_fullvoltage_allHits	16	LEAP 5000-XR	Ruttan	40pJ	08458	Full Voltage	3.47	48.54	all hits	0.045188	4	1
Ruttan_XR_8458_40pJ_fullvoltage_singleHits		LEAP 5000-XR	Ruttan	40pJ	08458	Full Voltage			single hits	0.044121	-20	0
80 pJ, Constant Ion Ratio, $^{32}S^{1+}/^{32,32}S_2^{1+}$ = 1:1												
Balmat_XR_9023_fullvoltage_allHits	26	LEAP 5000-XR	Balmat	S^+/S_2^+=1:1	09023	Full Voltage	3.46	49.23	all hits	0.045829	18	22
Balmat_XR_9023_fullvoltage_singleHits		LEAP 5000-XR	Balmat	S^+/S_2^+=1:1	09023	Full Voltage			single hits	0.044806	-4	24
Ruttan_XR_9021_fullvoltage_allHits	20	LEAP 5000-XR	Ruttan	S+/S2+=1:1	09021	Full Voltage	3.62	47.1	all hits	0.044894	-2	-5
Ruttan_XR_9021_fullvoltage_singleHits		LEAP 5000-XR	Ruttan	S+/S2+=1:1	09021	Full Voltage			single hits	0.043822	-26	-7

IVAS

				Standard	Mineral	Formula	$^{34}S/^{32}S$	$\delta^{34}S$ (CDT)	
Canyon Diablo Troilite				**Canyon Diablo**	**Troilite**	**FeS**	**0.045005**	**0**	
Ruttan Pyrite				**Ruttan**	**Pyrite**	**FeS2**	**0.045059**	**1.2**	
Balmat Pyrite				**Balmat**	**Pyrite**	**FeS2**	**0.045684**	**15.1**	

80 pJ, Varying Ion Ratio	**Instrument**	**Standard**	**Dataset**	**Voltage Range**	**Fe++/Fe+**	**Data type**	**$^{34}S/^{32}S$**	**$\delta^{34}S$ (model CDT)**	**$\delta^{34}S$ (Ruttan)**
Balmat_XR_8493_80pJ_fullvoltage	LEAP 5000-XR	Balmat	08493	Full voltage	5.21	all hits	0.045565	12	29
Balmat_XR_11434_80pJ_fullvoltage	LEAP 5000-XR	Balmat	11434	Full voltage		all hits	0.045591	13	14
Ruttan_XR_8492_80pJ_fullvoltage	LEAP 5000-XR	Ruttan	08492	Full Voltage	5.77	all hits	0.044334	-15	-12
Ruttan_XR_11435_80pJ_fullvoltage	LEAP 5000-XR	Ruttan	11435	Full Voltage		all hits	0.045015	0	2
40 pJ, Varying Ion Ratio									
Balmat_XR_8462_40pJ_full voltage	LEAP 5000-XR	Balmat	08462	Full Voltage	3.23	all hits	0.046207	27	12
Balmat_XR_8460_40pJ_fullvoltage	LEAP 5000-XR	Balmat	08460	Full Voltage	3.48	all hits	0.046123	25	10
Ruttan_XR_8458_40pJ_fullvoltage	LEAP 5000-XR	Ruttan	08458	Full Voltage	3.47	all hits	0.045699	15	4
80 pJ, Constant Ion Ratio, $^{32}S^{1+}/^{32,32}S_2^{1+}$ = 1:1									
Balmat_XR_9023_fullvoltage	LEAP 5000-XR	Balmat	09023	Full Voltage	3.46	all hits	0.046126	25	19
Ruttan_XR_9021_fullvoltage	LEAP 5000-XR	Ruttan	09021	Full Voltage	3.62	all hits	0.045317	7	-2

Gaussian Fitting

	Standard	Mineral	Formula	$^{34}S/^{32}S$	$\delta^{34}S$ (CDT)
Canyon Diablo Troilite	**Canyon Diablo**	**Troilite**	**FeS**	**0.045005**	**0**
Ruttan Pyrite	**Ruttan**	**Pyrite**	**FeS2**	**0.045059**	**1.2**
Balmat Pyrite	**Balmat**	**Pyrite**	**FeS2**	**0.045684**	**15.1**

80 pJ, Varying Ion Ratio	**Instrument**	**Standard**	**Dataset**	**Voltage Range**	**Fe++/Fe+**	**Data type**	$^{34}S/^{32}S$	$\delta^{34}S$ (model CDT)	$\delta^{34}S$ (Ruttan)
Balmat_XR_8493_80pJ_fullvoltage	LEAP 5000-XR	Balmat	08493	Full voltage	5.21	all hits	0.044105	-20	20
Balmat_XR_8493_80pJ_fullvoltage	LEAP 5000-XR	Balmat	08493	Full voltage		single hits	0.043620	-31	15
Ruttan_XR_8492_80pJ_fullvoltage	LEAP 5000-XR	Ruttan	08492	Full Voltage	5.77	all hits	0.043298	-38	-3
Ruttan_XR_8492_80pJ_fullvoltage	LEAP 5000-XR	Ruttan	08492	Full Voltage		single hits	0.043009	-44	1
40 pJ, Varying Ion Ratio									
Balmat_XR_8462_40pJ_full voltage	LEAP 5000-XR	Balmat	08462	Full Voltage	3.23	all hits	0.044596	-9	8
Balmat_XR_8462_40pJ_fullvoltage	LEAP 5000-XR	Balmat	08462	Full Voltage		single hits	0.044261	-17	11
Balmat_XR_8460_40pJ_fullvoltage	LEAP 5000-XR	Balmat	08460	Full Voltage	3.48	all hits	0.044277	-16	1
Balmat_XR_8460_40pJ_fullvoltage	LEAP 5000-XR	Balmat	08460	Full Voltage		single hits	0.043839	-26	11
Ruttan_XR_8458_40pJ_fullvoltage	LEAP 5000-XR	Ruttan	08458	Full Voltage	3.47	all hits	0.044243	-17	22
Ruttan_XR_8458_40pJ_fullvoltage	LEAP 5000-XR	Ruttan	08458	Full Voltage		single hits	0.043376	-36	25
80 pJ, Constant Ion Ratio, $^{32}S^{1+}/^{32,32}S_2^{1+}$ = 1:1									
Balmat_XR_9023_fullvoltage	LEAP 5000-XR	Balmat	09023	Full Voltage	3.46	all hits	0.044460	-12	25
Balmat_XR_9023_fullvoltage	LEAP 5000-XR	Balmat	09023	Full Voltage		single hits	0.044103	-20	29
Ruttan_XR_9021_fullvoltage	LEAP 5000-XR	Ruttan	09021	Full Voltage	3.62	all hits	0.043412	-35	-8
Ruttan_XR_9021_fullvoltage	LEAP 5000-XR	Ruttan	09021	Full Voltage		single hits	0.042895	-47	-12